

Solution-Grown Organic and Perovskite X-Ray Detectors: A New Paradigm for the Direct Detection of Ionizing Radiation

Laura Basiricò, Andrea Ciavatti, and Beatrice Fraboni*

The recent years witnessed an unprecedented enhancement in improved functionality materials and in the sophistication of solution-based device fabrication techniques. Such significant advancements lead to unexpected and effective opportunities for the utilization of solution-grown organic materials and perovskites in the detection of ionizing radiation. This review presents an updated overview of the recently reported top performing and more innovative organic/perovskite-based X-ray detectors, providing a comparison and a critical discussion on the different materials' properties and performance. Solution-growth methods that allow to obtain detector grade electronic materials are discussed, focusing on the growth both of single crystals and of thin/thick films and foreseeing the implementation of large-area, organic/hybrid-, and perovskite-based radiation detectors. Insights into the X-ray detection mechanisms are provided, detailing the fundamental processes involved in the charge collection and in the photoconductive gain model, together with the typical figures of merit that describe radiation detector performance.

Currently available radiation detectors are fabricated from inorganic semiconducting materials such as silicon, germanium, cadmium telluride, cadmium zinc telluride (CZT) which, while exhibiting impressive detector performances, do suffer from limitations, such as the difficulty to grow large-size, high-quality crystals at a low cost, and the difficulty to process them into large-area pixelated detector matrixes, possibly onto flexible, curved substrates. Such limitations prompted the search for alternative materials that could provide innovative and effective solutions for a wide range of applications, spanning from industrial testing, to civil security and to medical diagnostics and therapy.^[1–4]

Ionizing radiation can be detected with two different categories of functional materials, that is, scintillators and semiconductors, via an indirect or direct detection mechanism, respectively. In the indi-

rect detection, the incoming ionizing radiation is transduced into an electrical output signal in a two-steps process: in the first step a scintillator transforms the incoming X-ray radiation into a visible photon and in the second step a photodiode converts it to an electrical signal. In the direct detection mode, typically carried out by a semiconducting material, the incoming ionizing radiation is directly transduced into charge carriers and thus into an electrical output signal. In this review we will focus our attention on novel organic/hybrid semiconductors and perovskites for the direct detection of ionizing radiation.

The main requirements for a good direct semiconductor detector are briefly detailed below: i) high resistivity and low leakage current (critical for low noise operation); ii) a small enough band gap to grant a low electron–hole ionization energy, a large number of photogenerated electron–hole pairs and thus a higher signal to noise ratio; iii) a high atomic number (Z) and/or a large interaction volume for efficient radiation–atom interactions and thus effective detection; iv) high intrinsic $\mu\tau$ (mobility–lifetime) product, as an efficient collection of photogenerated charges is determined by which fraction effectively traverses the detector and reaches the electrodes; v) homogeneous, defect-free or defect-controlled materials, to ensure good charge transport properties and no conductive short circuits between the electrodes; vi) electrodes which produce no defects, impurities, or barriers to the charge collection process and which can be used effectively to apply a uniform electric field across the device.


It is obvious that not all of the above requirements can be easily met by a single material, but the dramatic advancements

1. Introduction

The past decade has witnessed a relevant increase in the use of ionizing radiation detectors in many aspects of modern society, leading to a growing demand for innovative, low cost detecting devices. The unprecedented rise in the number of novel improved functionality materials and in the sophistication of solution-based device fabrication techniques has led to unexpected and effective opportunities for the utilization of organic materials and perovskites in the detection of ionizing radiation.

Dr. L. Basiricò, Dr. A. Ciavatti, Prof. B. Fraboni
Department of Physics and Astronomy
University of Bologna
Viale Berti Pichat 6/2, Bologna 40127, Italy
E-mail: beatrice.fraboni@unibo.it

Dr. L. Basiricò, Dr. A. Ciavatti, Prof. B. Fraboni
National Institute for Nuclear Physics - INFN Section of Bologna, Italy

 The ORCID identification number(s) for the author(s) of this article can be found under <https://doi.org/10.1002/admt.202000475>.

© 2020 The Authors. Published by Wiley-VCH GmbH. This is an open access article under the terms of the Creative Commons Attribution License, which permits use, distribution and reproduction in any medium, provided the original work is properly cited.

The copyright line for this article was changed on 7 October 2020 after original online publication.

DOI: 10.1002/admt.202000475

in the functional properties and optoelectronic performance of organic/hybrid semiconductors thrust them forward as outstanding candidates for the alternative class of materials able to overcome the limitations of inorganic semiconductors while satisfying the main requirements for a radiation detector.^[5,6]

Organic and perovskite semiconductors are actually characterized by quite different atomic structures and properties.

The research activity on hybrid compounds in the past few years has thrived around a family of halide perovskites with composition of ABX_3 (where A is $CH_3NH_3^+$ (MA^+), $HN=CHNH_3^+$ (FA^+), or Cs^+ ; B is Pb^{2+} , Sn^{2+} ; X is Cl^- , Br^- , and I^-) or $A_2MM'X_6$ (where M is Cu^+ , or Ag^+ , M' is Bi^{3+} , Ga^{3+} , or In^{3+}). Such compounds have attracted lots of attention thanks to their excellent performance in solar cells, light-emitting diodes, lasers and photodetectors during the past few years.^[7–10] Halide perovskites were recently reported to be very good ionizing radiation detector materials,^[11,12] due to the large mobility and long carrier recombination lifetime (the $\mu\tau$ products of MAPbI₃ and MAPbBr₃ single crystals are comparable to that of CZT crystals), the tunable bandgap and the large radiation absorption coefficient, even in the form of polycrystalline films made from solution.^[13–16] The typical MAPbI₃ halide perovskite has a density of around 4 g cm^{-3} , providing a large linear attenuation coefficient of 10 cm^{-1} to 100 keV X-rays, comparable to that of CZT.

However, there still are quite a few challenges to overcome, such as how to stabilize the material and interface electrical properties under large bias and how to increase its stability in time and atmosphere.

Organic semiconductors, on the other hand, are materials composed mostly of carbon and hydrogen and combine the electronic advantages of semiconducting substrates with the ability to easily modify their chemical, physical, and electronic

properties and control their film-forming mechanisms through conventional wet chemistry. Thanks to the lack of highly toxic components, for example, heavy metals, organic semiconductors are considered as biocompatible and environment-friendly materials.^[17] Recent reports indicate how well performing radiation detectors can be realized based on organic semiconductors, either composed of small molecules (e.g., of 6,13 bis(triisopropylsilyl)ethynyl)pentacene (TIPS-pentacene)^[18–22] or conjugated polymers (e.g., poly(triarylamine) (PTAA)),^[23–26] However, their low density can be a limitation in terms of radiation absorption coefficient, for example, for TIPS-pentacene it is 0.2 cm^{-1} @100 keV, and a number of solutions have been proposed, ranging from adding high Z nanostructures blends of conjugated polymers and small molecules to directly tailoring the organic small molecule inserting high Z atoms.^[27,28] Organic semiconductors have by now become quite reliable electronic grade materials, employed for the fabrication of large-area organic electronics foils (often via low-cost printing processes) thanks to their good stability in time and atmosphere and good tolerance to bias stress. An additional, very relevant property of organic materials is their tissue-equivalent density, that allows to avoid calibration procedures or correction factors otherwise needed when measuring the radiation dose delivered to biological species with inorganic detectors.^[29,30]

The extremely relevant advances reported in the last years in the use of organic and perovskite semiconductors as direct X-ray detectors are summarized in **Figure 1**, showing the tremendous increase recorded for the radiation sensitivity, one of the most relevant parameters that characterize the performance of radiation detectors. The results are reported distinguishing organic (blue) and perovskite (orange) materials and their either single crystal (open symbols) or film (solid symbols)

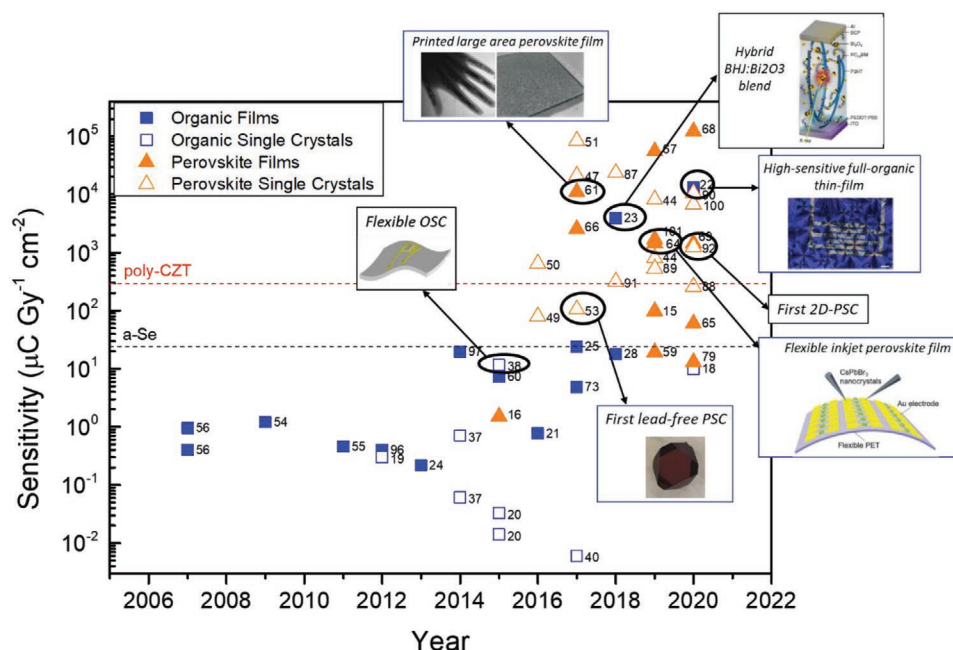


Figure 1. Timeline of the sensitivity of organic/hybrid and perovskite direct X-ray detectors developed. Flexible OSC: Adapted with permission.^[38] Copyright 2015, Wiley-VCH. First lead-free PSC: Adapted with permission.^[53] Copyright 2017, Springer Nature. Printed large area perovskite film: Adapted with permission.^[61] Copyright 2017, Springer Nature. Hybrid BHJ:Bi₂O₃: Adapted with permission.^[23] Copyright 2018, Springer Nature. Flexible inkjet perovskite film: Adapted with permission.^[64] Copyright 2019, Wiley-VCH. High-sensitive full-organic thin-film: Adapted with permission.^[22] Copyright 2020, Springer Nature.

form. The clearly identifiable message is that the enhancement in performance invests all 4 types of X-ray detectors that we will discuss in detail in this review, thanks to the thriving ongoing research activity and to its impressive success.

In this review we first present solution-growth methods that allow to obtain detector grade electronic materials both for organic/hybrid and perovskite materials. We distinguish the methods on the basis of the final thickness of the material: either single crystal or thin/thick film (a distinction that we will keep throughout the whole review). We proceed to discuss the different device architectures and their role in the radiation detection processes. We provide insights into the X-ray detection mechanisms, detailing the fundamental physics involved in the charge collection and in the photoconductive gain model, together with the figures of merit used to describe a detector performance. We then present an updated overview of the recent top performing and more innovative organic/perovskite-based X-ray detectors, providing a comparison and a critical discussion on the different materials properties and performance. Finally, we briefly illustrate the implementation of large-area, organic/hybrid- and perovskite-based radiation detectors and their use as imagers.

2. Growth Methods

This section briefly describes the reported solution-based growth methods for organic/hybrid and perovskite direct X-ray detectors. **Figure 2** shows a schematic summary of functional materials, structures and fabrication methods for this class of devices.

2.1. Single Crystals

Since the early 2010's, the interest about the employment of organic single crystals (OSCs) as active material for direct

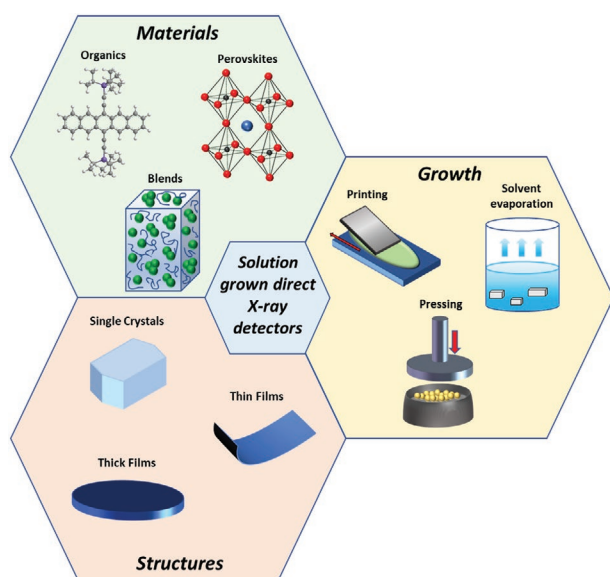


Figure 2. Schematic summary of active layer's materials, structures, and fabrication methods for organic/hybrid and perovskites direct X-ray detectors.

ionizing radiation detectors has raised, boosted by the development of the solution-growth processes, allowing easy fabrication of large and good quality crystals.^[31,32] Around the same time, in 2013, Stoumpos et al.^[33] reported the first perovskite single crystals (PSCs) for high-energy radiation detection, demonstrating the response to X-rays of 7 mm diameter CsPbBr₃ crystal ingots achieved by the vertical Bridgman method, a melt-growth method,^[34] using a three-zone furnace. However, large and high-quality (i.e., crack-free, with smooth surfaces, sharp borders, and optimum bulk transparency) perovskite single crystals can be grown from low-cost solution processes. Experienced procedures of solution growing of PSCs with high quality have been developed for photovoltaic applications and subsequent applications of PSCs for ionizing radiation detection exploited such knowledge and experience.

The most used solution-growth methods for OSCs and PSCs, based on the high solubility of these molecules in organic solvents over a range of temperatures and pressures, are described in the following.^[35]

2.1.1. Slow Solvent Evaporation Method

Slow solvent evaporation (SSE) is probably the easiest OSCs' growing method (**Figure 3a**). According to this technique a solution of the desired compound is allowed to slowly evaporate in a not completely covered baker, forming a supersaturated solution.^[36] The crystal seeds spontaneously nucleate at the bottom of the baker, growing into larger crystals. Indeed, almost all the OSCs reported for direct detection of ionizing radiation have been grown through SSE. In fact, SSE grown 4-hydroxycyanobenzene (4HCB),^[19,37,38] 1,8-naphthaleneimide (NTI),^[19] and 1,5-dinitronaphthalene (DNN)^[20,37] mm-size free standing single crystals have been demonstrated to real-time directly detect X-rays and alpha particles^[39] with high performance. Pipan et al.^[40] developed a novel growth strategy, based on SSE, to obtain millimeter-long single crystals TIPS-pentacene for direct X-ray detection onto gold interdigitated electrodes patterned on flexible plastic substrates, via direct inkjet printing of precursor solutions (**Figure 3b**). In much detail, this method involves the deposition of solvophobic-fluorinated molecules by inkjet printing on the substrate and its shaping as a closed fence. This acts as a chemical confinement for the subsequent inkjet printed TIPS-pentacene solution and leads to the formation of single crystals after the slow solvent evaporation, avoiding solution spreading and the consequent formation of finely dispersed TIPS-pentacene polycrystals.

2.1.2. Temperature Reduction Technique

In temperature reduction technique a solution is gradually cooled at a controlled rate until supersaturation regime occurred with consequent crystal formation. Such method has been employed to grow Rubrene single crystals, with a volume of about 1 cm³, which were demonstrated for neutrons detection.^[41] Indeed, the same molecular crystal was already demonstrated for direct X-ray detection, in that case employing physical vapor deposition (PVD)^[42,43] (i.e., a no-solution

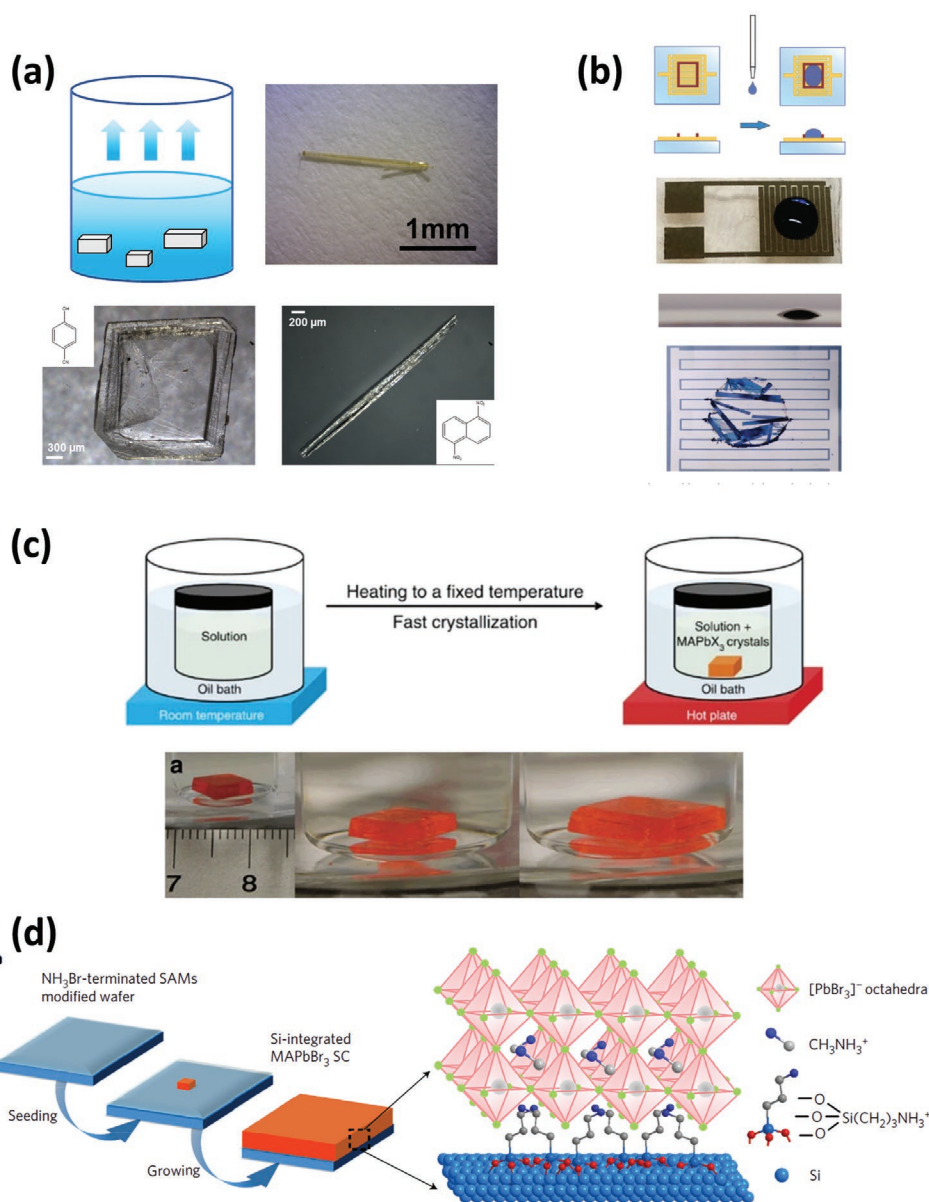


Figure 3. Solution-based crystallization methods for OSCs and PSCs growth for direct ionizing radiation detection. a) Sketch of the SSE method for the growth of some OSCs shown in optical pictures. Top (left): Reproduced with permission.^[19] Copyright 2012, Wiley-VCH. Bottom: Reproduced with permission.^[37] Copyright 2014, The Royal Society of Chemistry. b) Sketch of the inkjet printed “chemical fence confinement” approach exploiting SSE method for the growth of TIPS-pentacene OSCs onto pre-patterned flexible substrate. The pictures show top and side views of the TIPS-pentacene solution dropped onto PFDT-fenced interdigitated electrodes and the resulting crystals. Reproduced with permission.^[40] Copyright 2017, Wiley-VCH. c) Sketch of the ITC set-up for PSCs growth, in which the crystallization of vial is immersed in a heating bath. The pictures show ITC-grown MAPbBr₃ PSCs. Reproduced with permission.^[46] Copyright 2015, Springer Nature. d) Schematic illustration of the fabrication of Si-integrated MAPbBr₃ PSCs. Reproduced with permission.^[47] Copyright 2017, Springer Nature.

method) for the growth.^[20] Recently, 2D PSCs, with unique structural compatibility and tunability, have been grown by this method and successfully tested as X-ray detectors.^[44]

2.1.3. Antisolvent Liquid Diffusion Method

In the antisolvent liquid diffusion method, an opportune antisolvent is progressively added in controlled amounts to the

desired solution, causing gradual lowering of the solubility of the compound to be crystallized, and then its crystallization.

2.1.4. Organic Flux Solid Solvent Method

Organic flux solid solvent method is generally applied to crystallize organic semiconductors with low solubility in most organic solvents. Organic molecules in powder form can be dissolved

in the melt of other organic semiconductors and then crystallized by lowering the temperature.^[45]

2.1.5. Antisolvent Vapor-assisted Crystallization Method

The antisolvent vapor-assisted crystallization (AVC) method was developed by Shi et al.^[48] and employed by Wei et al. to grow the first reported hybrid lead halide perovskite (MAPbBr₃ in this case) single crystal-based X-ray detector.^[49] According to this method, an appropriate antisolvent is slowly diffused into a solution containing the crystal precursors, leading to the growth of high quality single crystals. The authors^[49] obtained 2 mm-thick large crystals with an area up to 25 cm², paving the way for large-area array detector applications. Moreover, they found that UV–O₃ treatment of the top surface of an as-grown MAPbBr₃, effectively passivate these surface defects permanently, leading to improved optoelectronic and detection properties. The main drawback of the AVC method is the slow rate of the growth process, typically lasting a couple of days. For this reason, most of the works on PSCs-based ionizing radiation detection followed alternative growing methods. The antisolvent vapor-assisted crystallization, is effective also for growing of OSCs.

2.1.6. Inverse Temperature Crystallization Method

Inverse temperature crystallization (ITC) method, developed by Saidaminov et al.^[46] permits rapid solution growth of high-quality size- and shape-controlled perovskite single crystals (Figure 3c). It exploits the loss of solubility occurring in a specific solvent or solvents at elevated temperatures, that is, the retrograde solubility regime. Both hybrid (FAPbI₃,^[50] MAPbBr_{3-x}Cl_x^[51]) and inorganic (CsPbBr₃^[52]) lead halide PSCs ITC grown have been successfully employed for ionizing radiation detection. In addition, lead-free Cs₂AgBiBr₆ and Cs₃Bi₂I₉ SCs X-ray detectors, solution-grown by modified ITC method, have been recently reported.^[53] Interestingly, some studies reported strategies about modification of standard processes to tune the physical properties of the material for high energy photons detection.

Wei et al.^[47] developed a novel solution-process technique to monolithically integrate MAPbBr₃ single crystals onto Si substrates at low temperature, providing the proof of integration of the crystals with thin-film transistors to form active-matrix flat-panel imagers for medical imaging application. To obtain strong mechanical adhesion and good electrical contact between MAPbBr₃ single crystals and Si wafers, the authors added a NH₃Br-terminated self-assembled monolayer (SAM) on the Si surface. Through hydrolysis and condensation processes, the SAM acts as a strong bonding-bridge between Si substrate and MAPbBr₃ crystals, overcoming the weakness of hydrogen bonds and van der Waals interactions that would be obtained with a direct growth of PSC on not-treated Si surface (Figure 3d). A pre-seeded MAPbBr₃ single crystal with dimensions of <300 μm was placed onto the wafer, modified with NH₃Br-terminated molecules, and grown to a sufficient thickness to absorb the most of the impinging X-rays (i.e., 2–3 mm

for 50 keV radiation) with a modified ITC. Applying this strategy a MAPbBr₃ single crystal with an area of 5.8 mm × 5.8 mm, integrated onto the Si wafer has been obtained, which can sustain its own gravity plus an added weight of 10 g.

2.2. Thick/Thin Films

The solution-based deposition technique used for the realization of thick/thin films as active materials for X-ray detection are basically the same for both perovskite and organic materials. Some are more suitable for deposition of thick films, some for thin films and others allow the tuning of the layer thickness by control the deposition parameters.

2.2.1. Spin Coating

Spin coating is a very easy and common solution-based deposition techniques for organic and perovskite-based electronics. Therefore, it has been extensively employed also for fabrication of organic,^[54,55] hybrid,^[23–25] and perovskite^[15,16]-based X-ray detectors. In particular, the first thin-film perovskite-based X-ray detector was demonstrated by Yakunin et al.^[16] in 2015, who reported the detection performance of a p-i-n photodiode consisted of four spin-cast layers, including MaPbI₃ active layer with a thickness in the range (260–600) nm. This method involves the dropping of the solution onto the desired substrate, which is then accelerated to a high angular velocity through a rotating plate. Upon solution spreading and solvent evaporation a uniform film is formed, typically exhibiting a homogeneous thickness, depending on the solution concentration, and density and on the spin speed. Despite the high quality of the achievable thin films, spin coating suffers from the intrinsic limit of being scarcely scalable to large substrates and lack of reproducibility for thick films that involve low spin speed.

2.2.2. Printing Techniques

The printing techniques are here intended as the additive solution-based deposition processes enabling large area coverage, and therefore scalable for potential use in mass production. Among such methods, the method of drop casting is a type of solvent evaporation technique where a drop of solution is cast onto the desired substrate and then the solvent is let drying, with the formation of microcrystalline thin-film (or either single crystals as discussed above for SSE method) upon solute precipitation. Due to its easiness and effectiveness, it has been widely employed for thin film-based ionizing radiation detectors. Indeed, the first reported organic thin-film direct X-ray detector^[56] employed a 2 μm thick polymer active layer deposited by drop-casting. More recently, different studies on the X-ray photoconversion mechanism in full-organic thin films have been carried out by employing drop cast devices.^[21,28] Thanks to the low-temperature process required by drop-casting due to the use of low boiling point solvents, such devices have been demonstrated as reliable flexible and wearable detectors^[30] (Figure 4a). In addition, drop-casted CsPbBr₃

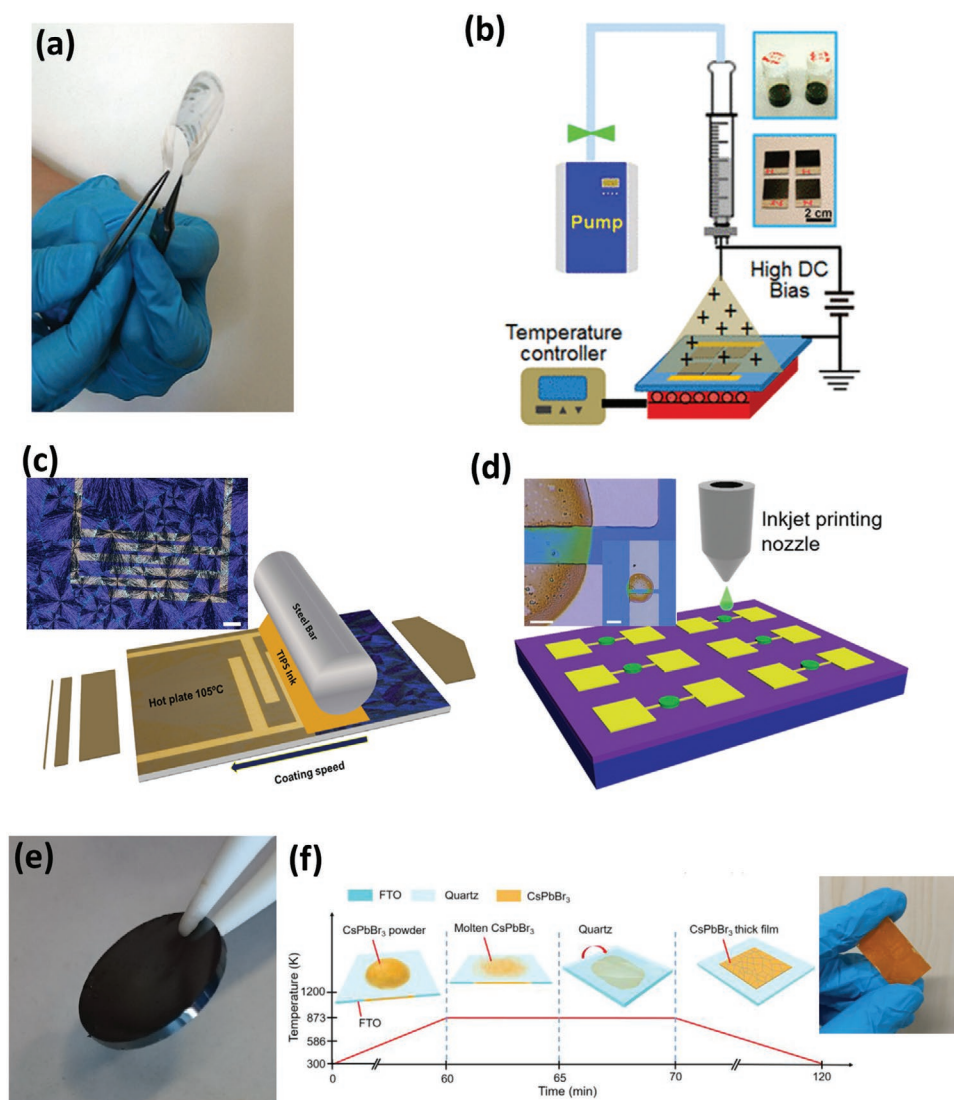


Figure 4. Solution growth methods for thick/thin film based organic, hybrid, and perovskite-based X-ray detectors. a) Picture showing the flexibility of drop casted organic thin film-based X-ray detectors. Reproduced with permission.^[21] Copyright 2016, Springer Nature. b) Schematic of the electro-spray deposition and pictures of the resulting Cs_2TeI_6 solutions and films. Reproduced with permission.^[59] Copyright 2019, American Chemical Society. c) Sketch of the BAMS deposition setup and picture of the resulting organic thin film. Reproduced with permission.^[22] Copyright 2020, Springer Nature. d) Schematic for perovskite QD-based devices inkjet printing procedure and optical image of device with printed QDs film. Reproduced with permission.^[64] Copyright 2019, Wiley-VCH. e) Free-standing MAPbI_3 wafer (0.5 in. \times 1 mm) grown by mechanical sintering process. Reproduced with permission.^[66] Copyright 2017, Springer Nature. f) Process schematic for a thick CsPbBr_3 film using the four-step hot-pressing method. Reproduced with permission.^[67] Copyright 2019, Wiley-VCH.

microcrystalline perovskite layer, few micrometer thick, inorganic perovskites have been recently assessed for clinical radiotherapy dosimetry.^[57]

Spray coating is based on the ejection from a nozzle of small droplets aerosolized by an inert carrier gas.^[58] The aerosolized particles then hit the substrate and dry rapidly, forming homogeneous films with tunable thickness by varying the deposition parameters (pressure, concentration, density) and duration time. Yakunin et al.^[16] were the first reporting on thick film-based perovskite X-ray detectors, using MaPbI_3 -based solution spray-coated on glass substrate to obtain 10–100 μm thick perovskite films. One of the several variations of spray coating is electro-spray deposition, where the aerosol droplets are formed

by means of the Coulomb repulsion and guided by the electrical gradient between the nozzle and the substrate. This technique has been recently employed^[59] for the deposition of inorganic (Cs_2TeI_6) perovskite 25 μm thick film for X-ray detection (Figure 4b). The authors studied in detail how to control and tune the spray parameters (distance and electric field between the nozzle and the substrate, solution ratio) and substrate temperature to properly engineer the perovskite's morphology and thickness for optimized high-energy radiation detection. Spray coating has been proposed as fabrication techniques also for X-ray detectors based on hybrid organic/inorganic bulk heterojunction blended with PbS quantum dots (QDs)^[26] or scintillator particles.^[60] Meniscus-guided coating refers to a class of

printing deposition techniques where a solution meniscus is linearly translated either by moving the substrate or the coating tool (e.g., bar, blade, capillary etc.) to align the crystallites of the deposited film^[58] along the direction of the guiding motion. In fact, the meniscus acts as air-liquid interface for crystallization upon solvent evaporation, allowing the directional alignment of the growing crystallites. Doctor blade, utilizing a blade as coating tool, is probably the most diffuse of this class of techniques since it has been adapted to roll-to-roll printing processes and thus envisages mass customization. In 2017 Kim et al.^[61] demonstrated the first printable perovskite large-area, low-dose X-ray imager, in which the absorbing layer was a 830 μm thick polycrystalline MAPbI₃ film deposited by a doctor blade. More recently, a novel modified solution shearing technique, that is, bar-assisted meniscus shearing method (BAMS)^[62,63] has been employed for the fabrication of organic thin-film X-ray detectors, using a blend solution of TIPS-pentacene and polystyrene (PS)^[22] (Figure 4c). The authors demonstrated how BAMS is an effective tool to tune the carrier mobility by controlling the TIPS-pentacene:PS blending ratio, and the grain size and grain boundaries density via regulation of the coating speed, achieving exceptionally high sensitivity to X-rays.

Inkjet printing is an additive patterning technique involving the ejection of a droplet of solution from a chamber reservoir through piezoelectric or thermal actuators, directly on the substrate. The small amount of material delivered makes inkjet printing suitable for low temperature (<100 °C) thin film deposition onto thin plastic substrates for flexible electronics. Both inorganic^[64] and hybrid^[65] perovskite X-ray detectors inkjet printed onto flexible substrate have been demonstrated in literature. In particular, Liu et al.^[64] reported on the first inkjet-printed 20 nm thick CsPbBr₃ perovskite quantum dots (Figure 4d) as active layer of X-ray detector arrays, fabricated onto large-area polyethylene terephthalate (PET) substrate.

2.2.3. Pressing and Melt Methods

Despite pressing/melt methods could not properly be considered solution-based techniques, they have been effectively used to fabricate thick-film based direct ionizing radiation detectors and thus deserve a brief mention here. Moreover, solution-grown micro-crystals/powders are often employed as starting structures to be pressed for the fabrication of thick films and wafers. In 2017 Shrestha et al.^[66] reported on high-performance direct X-ray detectors based on sintered hybrid lead triiodide perovskite wafers. Their method involves the preliminary synthesis of MAPbI₃ microcrystals by precipitation of a precursor solution. This process leads to 50 nm⁻¹ μm size shape-irregular microcrystals, that subsequently undergo to a pressure of 0.3 GPa for 5 min by a hydraulic press, leading to the formation of a compact MAPbI₃ wafer (Figure 4e). The as-fabricated perovskite wafers are (0.2–1) mm thick, with a low roughness of 75 nm and a density near that of MAPbI₃ single crystals even though the grain boundaries between the microcrystals are still well identifiable in the wafer. A couple of years after, Pan et al.^[67] proposed a hot-pressing method to fabricate quasi monocrystalline inorganic perovskite CsPbBr₃ thick (several hundreds of microns) films. The method consists of four steps (Figure 4f). In the first step

CsPbBr₃ powder is placed onto a fluorine-doped tin oxide (FTO) glass and heated at 873 K for 5 min. This procedure gives rise to a melt perovskite layer uniformly covering the FTO (second step). In the third step a pre-heated quartz is used to press the molten layer, and it is removed in the last step after the slow decreasing of the temperature. Further, very recently, a heat-assisted high-pressure press method has been demonstrated for MAPbI₃ wafer fabrication^[68] for X-ray detection. In addition, Matt et al.^[69] demonstrate direct X-ray detection by crystalline CsPbBr₃ 250 μm thick films fabricated via melt processing. This method involves the distribution of microcrystalline CsPbBr₃ onto FTO-covered glass substrate, its heating up to 575 °C and then the slow-cooling at room temperature.

Among organic/hybrid film-based X-ray detectors, to the best of our knowledge, the work of Jayawardena et al.^[70] is the first reporting a pressing fabrication method. Hybrid organic-inorganic P3HT:PCBM:Bi₂O₃ (P3HT stands for poly (3-hexylthiophene) and PCBM for [6,6]-phenyl-C61-butyric acid methyl ester) powder was prepared through solution-process and then pressed by means of a hydraulic press with a 1000 kg loading for 15 min at room temperature, resulting in 250 μm thick pellets.

However, despite high performing X-ray detectors based on perovskite and organic thick films have been demonstrated, the employment of such growth technique is high energy consuming and not compatible with plastic flexible substrates due to the high temperature involved.

3. Device Architectures

The organic, hybrid, and perovskite direct ionizing radiation detectors reported in literature can be grouped in three general device architectures, similarly to visible light detectors:^[71] photoconductors, photodiodes and phototransistors (Figure 5). Photoconductors and photodiodes are 2-terminal architectures where the absorbing material is between two conductive electrodes, generally metals. The geometry can be either vertical, that is, the absorbing layer is sandwiched between the electrodes, or co-planar, that is, the active layer is directly exposed to the impinging radiation and laterally interfaced with the electrodes. The vertical geometry is widely used for its convenience in the integration with pixelated matrix, however, lateral co-planar is useful for the ease of fabrication and the need of low driving voltage since the intensity of the electric field depends only on the electrode spacing and not on the layer thickness.^[72] Photodiode architecture benefits from the large knowledge coming from the organic/hybrid photovoltaics research carried on in the last decade. Moreover, by operating the diode in reverse polarization, it allows the reduction of the dark current and, in principle, the enhancement of the signal-to-noise ratio and limit of detection. Phototransistors constitute a less explored geometry for X-ray detectors, reported so far only for thin film organic-based devices.^[22,28,73] In a phototransistor the charge current flowing within the channel, that is, between the source and drain electrodes, is tuned not only by the polarization of a third electrode (gate) (as in a simple field effect transistors), but also by the additional charges induced by the interaction with the radiation. Therefore, the X-ray detection performance can be tuned by properly choosing the biasing conditions of the transistor.

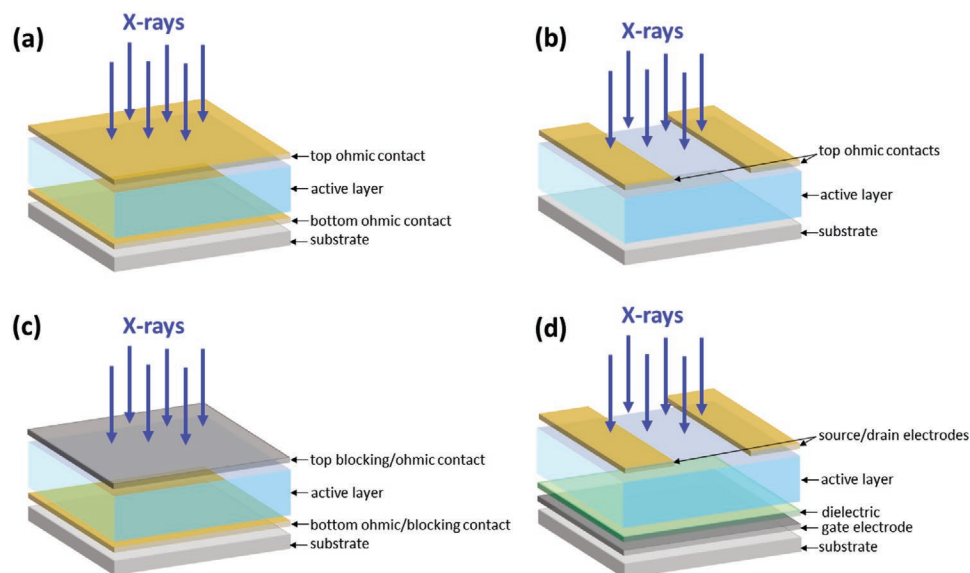


Figure 5. Schematics of four typical architectures for direct X-ray detectors. a) Vertical photoconductor architecture; b) co-planar photoconductor architecture; c) photodiode architecture; d) phototransistor architecture.

Biasing the gate electrode with voltages progressively higher than the threshold, the charge density in the transistor channel increases, bringing to the enhancement of charge accumulation and gain of the detection performance. On the other hand, by setting the gate biasing in under-threshold, the charge carrier density in the transistor channel is low and the photocurrent results from the separation and collection of ionization charges generated by X-ray photon absorption. The advantage of this structure lies in its ability to fully control the signal by the gate voltage, which offer the possibility to avoid the thin film transistor (TFT) switch at the pixel level, in large-area direct conversion X-ray imaging.^[74]

In the three detector structures described above, the X-ray photoconversion process can vary, depending on the operational parameters and materials' properties. In the following a brief description of the two main detection mechanism in such classes of detector is reported: charge collection and photoconductive gain processes. Often the devices exhibit a mixed behavior, where the two mechanisms coexist and/or are selectively activated by operative conditions, as will be discussed in the next section.

4. X-Ray Direct Detection Mechanism

Generally speaking, when an X-ray photon interacts with a semi-conducting material, it creates a high-energy electron which then deposits its excess energy in the surroundings by photoelectric effect and Compton scattering process, leading to the formation of electron-holes pairs and phonons.^[6] If an electric field is applied to the system, the electron-hole pairs are separated and collected by the respective electrodes, leading to the direct conversion of the incident photons to an electrical current (**Figure 6a**). This process is commonly referred as current mode operative regime, typical of dosimeters and medical imagers.

The magnitude of the maximum photocurrent I_{CC} , accounting for such a carrier generation and collection process, is described by:

$$I_{CC} = \Phi nq \quad (1)$$

where q is the elementary charge, Φ is the photon absorption rate, n is the number of the generated electron-hole pairs per absorbed photon.^[6,21]

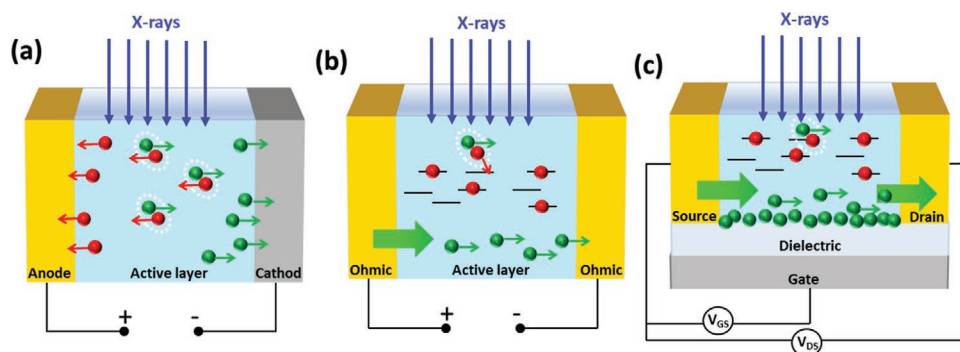


Figure 6. Schematics of the direct X-ray detection processes. a) Charge collection in photodiode architecture. b) Photoconductive gain in photoconductor architecture. c) Photoconductive gain in phototransistor architecture.

The photon absorption rate Φ can be calculated from the Lambert-Beer equation:

$$\Phi = \Phi_0 [1 - \exp(-\mu_0 t)] \quad (2)$$

where: $\mu_0 = \mu/\rho \cdot \rho_0$ is the linear attenuation coefficient, with μ/ρ indicating the mass attenuation coefficient of the absorbing material, ρ_0 its density, t is the interaction length with the material and Φ_0 is the incident photon flux. On the other hand, direct ionizing radiation detectors for photocounting and spectroscopy applications usually work in voltage mode. In this case the radiation induced hole–electron pairs correspond to charges that are counted in a single voltage pulse, with an intensity proportional to the photon energy. Since the counting mode is mainly used in γ -ray and charge particles detectors, and we here focus on organic/hybrid and perovskite materials for X-ray detection, the detailed discussion of this operation mode goes beyond the scope of this review.

4.1. Charge Collection

Due to the high purity and low defect and trap density of the materials used as active detective medium, the charge collection is the dominant process in direct X-ray detection, both in PSC and OSC-based devices.

Also, in polycrystalline film-based photodiodes the detection of high-energy photons is ruled by charge collection, due to the inhibition of injection in depletion regime.

The detailed description of the induced current by a moving charge toward a collecting electrode have been provided by Shockley^[75] and Ramo.^[76] They introduced the concept of weighting field, that describe the relationship between the charge collection and instantaneous position of carriers. This description becomes important in multielectrode matrices and arrays, where an efficient shaping of electric field and reduction of crosstalk between adjacent pixels are highly recommended.

4.2. Photoconductive Gain

Photoconductive gain is a physical phenomenon typical of photoconductors, where the semiconducting photoactive material is between two ohmic contacts (or injecting contacts)^[6] (Figure 6b). Such mechanism amplifies the photo-generated current by a factor G , leading to photo-to-electrical efficiency exceeding 100% and providing high sensitivity to the radiation. It occurs when radiation-generated, free charge carriers accumulate and pass several times through the semiconductor between the electrodes before recombination sets in. This process of amplification is activated by the trapping of minority charge carriers and the factor G can be expressed as the ratio between the recombination time τ_r , characteristic of the trapped states, and the transit time τ_t of free moving carriers:

$$G = \frac{\tau_r}{\tau_t} = \frac{\mu V \tau_r}{L^2} \quad (3)$$

Where μ is the charge mobility, V is the applied bias and L is the distance between the two electrodes, considering a uniform electric field.

τ_r and τ_t represent respectively the time of recombination of the minority carriers trapped in the active layer, that is, the minority carrier lifetime, and the transit time of the majority carriers to drift along the detector's active layer.

A photoconductive gain mechanism has been proposed to interpret the high X-ray induced conductivity in organic thin-film photoconductors, based on TIPS-pentacene and derivatives.^[21] A high atomic number (Z) and/or a large interaction volume for efficient radiation–atom interactions are necessary requirements for high-sensitivity and high efficiency X-ray detectors, since the cross-section for photoelectric absorption in a material of atomic number Z varies as Z^n , where $4 < n < 5$. However, organic thin film-based X-ray detectors are intrinsically characterized by a low Z and a small interaction volume, leading to extremely low X-ray absorption (about 0.0015% for 100 nm thick TIPS-pentacene films). Therefore, a gain mechanism must be taken into account to describe the X-ray induced photocurrent observed for this class of materials. Since TIPS-pentacene is a p-type material, a different behavior can be assumed for holes and electrons generated by the interaction with the X-rays. Holes drift along the active layer reaching the collecting electrode while electrons get trapped and act as ‘doping centers’. Due to the ohmic nature of the electrical contacts, charge neutrality is ensured in the device, therefore for every hole collected, another is re-injected. Therefore, for each electron-hole pair created, more than one hole contributes to the X-ray induced photocurrent before recombination takes place, resulting in the photoconductive gain effect. The authors proposed also an analytical kinetic model based on a stretched exponential behavior of the X-ray induced charge density, well-describing the slow recombination dynamics of X-ray generated carriers, resulting in organic thin films from the presence of deep trap levels which remove free electron from the recombination process. The authors reported a gain value up to 4.7×10^4 in such devices.

Yakunin et al.^[16] reported about a photoconductive gain in MAPbI₃, 60 μm thick film-based photoconductor, estimating a contribution to the observed sensitivity of a factor of at least 30. This gain value is higher than that measured for much thinner (500 nm) photoconductors under visible light. The authors tentatively attributed this behavior to a less favorable electric field distribution, higher trap density and smaller photoinduced charge density in the thicker perovskite films. Moreover, the signal they observed under X-rays is very fast, in contrast with the slower response times resulting from trap-assisted photoconductive gain detection process.

Besides photoconductors, phototransistors based on organic thin films have been demonstrated to detect X-rays with a high sensitivity due to an enhancement of the photoconductive gain effect through the gate polarization^[28,73] (Figure 6c). As mentioned in the previous section, the gate voltage sweeps to progressively switch ON the transistor, that is, towards more negative/positive values for p-type/n-type semiconductor, the charge density in the transistor's channel increases, leading to an enhancement of minority carriers accumulation and majority carriers conduction. Moreover, majority carriers are more easily injected

from the electrodes due to the lowering of the contact resistance. Further, in over-threshold condition τ decreases. All these effects correspond to a higher gain G of the X-ray induced photocurrent.

4.3. Figures of Merit

The complete picture of a detector is outlined by many parameters, that span from material to device properties. As illustrated in the introduction, the design of a good detector starts from the proper selection of active material, based on atomic number Z , $\mu\tau$ product, bandgap, and bulk resistivity. However, from a technological point of view, below we focus on sensitivity, dark current, detection limit, and time response, that are the most appropriate figures of merit to assess the potentiality of the final device.

4.3.1. Sensitivity

The X-ray sensitivity S is defined as the charge collected Q , per unit exposure of radiation X , per unit area A of incident radiation.

$$S = \frac{Q}{XA} \quad (4)$$

It describes the ability of a detectors to respond to a specific amount of radiation, that is, the output signal amplitude, that summarizes the overall direct detection process: from X-ray absorption to charge pairs creation, transport, and collection. For these reasons it is an important parameter to evaluate the performance of X-ray detectors. Following the approach of Kasap et al.,^[77,78] developed to describe X-ray photoconductor based on amorphous selenide (a-Se), the theoretical sensitivity can be evaluated considering the three steps of the detection process. The quantum efficiency η_x ($\eta_x = 1 - e^{-\mu_0 t}$, where μ_0 the linear attenuation coefficient and t the thickness of the active layer), describes the fraction of the incident radiation that is effectively absorbed by the detectors (often refereed also as attenuated fraction). It depends on the detector thickness, on the density and on the atomic composition of the materials, and it is strongly energy dependent. The second step is the generation of charges by the absorbed X-ray photons. The number of the electron-hole pairs created by each absorbed photon is the average absorbed energy divided by the, so called, electron-hole pairs creation energy W_{\pm} , typical of a specific material: the general expression is $\eta_m = \frac{E(\mu_{en}/\mu)}{W_{\pm}}$. The last stage is the charge transport and collection, that involve all the processes that allow the X-ray generated charges to be effectively collected at the electrodes. It is described by the parameters η_{CC} , charge collection efficiency, that depends on mobility-lifetime product, external electric field, and on geometrical design of the detector. Thus, given a specific material, the maximum theoretical sensitivity can be expressed as $S = S_0 \eta_x \eta_m \eta_{CC}$, where S_0 is a constant that depends only on the X-ray energy. Its value, as reported in Mescher et al.,^[65] is $S_0 = \frac{5.45 \times 10^{13} e}{E(\mu_{en}/\rho)_{air}} [\text{C R}^{-1} \text{cm}^{-2}]$, where e is the fundamental electron charge, E is the X-ray photon energy, $(\mu_{en}/\rho)_{air}$ the mass energy-absorption coefficient.

Therefore, the route to develop high sensitivity X-ray detectors passes through the delicate equilibrium of an high absorbing layer (high quantum efficiency), low W_{\pm} (high number of generated charge pairs), and superior electrical characteristics (efficient charge collection) that maximize the product $\eta_x \times \eta_m \times \eta_{CC}$.

The operative definition of sensitivity, for a detector operating in current mode, is the linear dependence of the X-ray photocurrent signal $\Delta I = I_{X\text{-ray}} - I_{\text{dark}}$ as function of impinging dose rate (DR):

$$S = \frac{1}{A} \frac{\partial(I_{X\text{-ray}} - I_{\text{dark}})}{\partial DR} \quad (5)$$

where I_{dark} is the dark current, $I_{X\text{-ray}}$ is the current under irradiation ($I_{\text{signal}} + I_{\text{dark}}$), DR is the dose rate (in Gy air kerma s^{-1}) or radiation exposure (in R s^{-1}), and A is the sensitive area of the detector.

It is generally expressed divided per unit area, but in literature it is often used also divided per unit volume, to compare the performance of novel radiation detectors. Therefore, attention must be paid in the comparison between the sensitivity values reported in literature, since the units of measure and the types of normalization reported can be very different. Overall, the use of sensitivity per unit area highlights the detection performance as an operational device, while the sensitivity per unit volume underlines the intrinsic material properties. In this view, the normalization per unit area has to be calculated considering the whole pixel area, and not the active channel area, that is, the product between the channel width and the channel length, to be fairer in the comparison between different geometries (e.g., vertical stacked structures) with respect of those which use interdigitated electrodes.

Typical sensitivity values of traditional inorganic semiconductors based on polycrystalline stabilized amorphous selenide (a-Se) and polycrystalline CZT, at photon energy of 20 keV, are $2.4 \times 10^{-1} \mu\text{C cm}^{-2} \text{R}^{-1}$ and $2.55 \mu\text{C cm}^{-2} \text{R}^{-1}$, respectively. The sensitivity values at photon energy of 60 keV are reported in Kasap et al.^[77] and Figure 1.

4.3.2. Dark Current

Another fundamental property of a radiation detector is the dark current I_{dark} , that is, the current flowing in absence of any radiation stimulus. An ideal detector should have the smallest possible dark current to reduce the noise. In fact, a small noise is essential as much as a strong output signal amplitude (defined by the sensitivity). The detector noise determines the lowest detectable dose (LoD, paragraph 4.3.3.), the signal-to-noise ratio (SNR), and the dynamic range, that are all significant figures of merit both for X-ray dosimeters and imagers. Even if several sources of noise could be identified, usually the most relevant one is the noise due to fluctuations of the dark current.

The main contributions to dark current arise from the presence of defective states, from thermal charge carrier generation in the bulk of the material and from the injection of carriers at the electrodes interface. The reduction of electrically active defects is obtained through the growth of high-quality

ultra-pure single crystals that are intrinsically low-defective materials, while in polycrystalline films, further passivation treatments (e.g., the addition of insulating polymers) are performed. A large energy gap hinders the thermal generation of charges from the bulk, a characteristic that is shared by many organic semiconductors employed as X-ray detectors. Finally, the creation of barriers that hinder the charge injection from the electrodes is a method used in photodiodes, through the deposition of blocking layers between the electrode and the absorbing layer. Also, photoconductor devices have proved to benefit from the insertion of thin insulating layers at the electrodes interface.

Clearly, the dark current depends on the applied electric field at the working conditions, therefore, highly resistive materials ($>10^9 \Omega$) are desirable to apply strong electric field (enhancing the charge collection efficiency) keeping the dark current low. An alternative approach is the employment of architectures that allow to efficiently collect charges at low voltage (like co-planar architecture)^[21] or in passive mode.^[15,16,79]

The acceptable level of dark current strongly depends on the typical photon flux used for the target applications, that span from extremely low doses for environmental monitoring to high doses for radiotherapy and nuclear plants. A rough quantitative estimation has been made by Kasap et al.,^[80] indicating an ideal value between 0.1–1 nA cm⁻². Following its suggestion, an acceptable value of 10 nA cm⁻² can be realistically considered for organic and perovskite detectors, due to their lower value of $W\pm$ in comparison with a-Se. Indeed, all the materials currently employed in commercially available detectors have dark current <50 nA cm⁻².

4.3.3. Limit of Detection

The detection limit quantifies the smallest signal that can be reliably identified. The assessment of the detection limit, or Limit of Detection (LoD), of devices is fundamental for the evaluation of detection performance because it defines the range of potential applications, as each of them demands for specific minimum detectable amount of dose. For instance, most of medical diagnostic systems require typical dose rates below 5.5 $\mu\text{Gy s}^{-1}$ (e.g., surgical monitoring, mammography),^[81,82] but the range spans from typical single exposure for CT scan (below $\mu\text{Gy s}^{-1}$ for few milliseconds) to high doses dispensed in radiotherapy (tens of mGy s^{-1} with total dose up to 5 Gy^[57]).

Despite the simplicity of the concept, a rigorous definition is tricky, so that in the literature numerous inconsistent and arbitrary definitions lead to very different LoD values. The most widely used definition arises from the IUPAC description^[83] that sets the detection limit for the concentration of an analyte in a test solution as three times the minimum precision. In other words, when applied to an electronic sensor, it is the minimum radiation that provides the $\text{SNR} = 3$. This simple, but approximated, value comes from the considerations made by Currie in 1968^[6,84] and its quantitative examples on radioactivity measurements. The quantitative analysis of Currie should be taken into accounts when more rigorous assessments are required. Three different levels have been identified, based on minimizing the probability to have false positive (i.e., detection where no signal is present), while keeping low also the possibility to have false negative (i.e.,

no detection when a real signal is present): L_C , critical level, the minimum value above which an observed signal has only 5% to be a false positive ($1.64 \sigma_{\text{dark}}$); L_D , detection limit, is the true signal level, above which the probability to have false negative is below 5% ($3.29 \sigma_{\text{dark}}$); L_Q , determination limit, is the value above which the precision of the measurements is high enough to be quantitative ($10 \sigma_{\text{dark}}$); L_Q is scarcely employed. Attention must be paid in the comparison of LoD for organic and perovskite X-ray detector reported up to now, because some works correctly follow the practical rule of $\text{SNR} = 3$, others instead report only the minimum detectable dose without any noise analysis or choosing an arbitrary value of SNR.

It is evident from the LoD definition that it strongly depends both on the signal amplitude (i.e., the sensitivity) and on the noise of the system (i.e., detector dark current and additional electronic noise), thus, a precise and independent evaluation of I_{dark} can greatly improve the LoD of the detection system.

4.3.4. Response Time

In a general definition, the response time quantifies the speed of the detectors. Its importance lies in the necessity to identify if a detector is applicable on a given field, where specific speed is requested. For instance, in medical imaging, fast detectors are desirable to minimize the time of X-ray exposure of the patients, while in dosimetry and environmental monitoring the speed is less crucial.

Most of the detectors show a signal profile that can be fitted with an exponential function with its own characteristic time. A more general, widely used, parameters are the operative definition of rise time, which is the time required by the signal to go from 10% to 90% of the full amplitude, and falling time, the time needed by the signal to relax at the starting dark level, when the radiation is switched off.

The rise time illustrates only the time of response upon the first radiation stimulus. However, also the falling time becomes important when the detection of multiple pulses is needed. The latter is often longer than the rise time, because it is more sensitive to long de-trapping times of defects in the material, thus increasing the dead time of the detector (i.e., the period where the detector it is not able to detect radiation) and limiting the maximum operation frequency.

Indeed, when the detection of multiple pulses is needed, the speed of the detector is conveniently expressed by a cut-off frequency, the maximum X-ray frequency at which the signal amplitude have been reduced to -3 dB with respect to the steady-state response. Sometimes, in datasheets of commercial detectors, the speed is given as the maximum frame-per-second (fps) that can be reliably detected. It is evident, like the detection limit, that the detector performance fixes the maximum limit, but the final rate of a full system strongly depends also on the readout electronics.

Other important parameters that contribute to fully characterize an X-ray detector are the linear dynamic range and the energy range, which indicate the meaningful range of X-ray dose rate and photon energies with a constant sensitivity. Large dynamic and energy range ensure accurate measurements over a large variation in dose rate and X-ray energy.

Moreover, the applied voltage and the power supply required to operate the detector play an important role when protection from electrical shock and low power consumption are crucial, like in the novel emerging applications towards portable and wearable devices.

5. Detection Performance

5.1. Single Crystal-Based X-Ray Detectors

5.1.1. Organic Single Crystals

Among organic materials, OSCs are ideal candidates as tissue-equivalent direct X-ray detectors thanks to their peculiar properties such as low Z, long-range molecular packing order, lack of grain boundaries, high charge mobility (up to $40 \text{ cm}^2 \text{ V}^{-1} \text{ s}^{-1}$), long exciton diffusion length (about $8 \mu\text{m}$) and transport anisotropy^[32] with respect to thin and thick organic film-based devices reported for this application.^[29,31] Moreover, they exhibit high resistivity and low dark currents due to the relatively large band gap which allows an effective charge collection even in photoconductor configuration, that is, without the need of a rectifying junction.

OSCs-based direct X-ray detectors were reported for the first time in 2012 by Fraboni et al. whose group assessed in the following years the reliability of different solution grown OSCs,

namely 4HCB,^[19,37,38] NTI,^[19] DNN,^[20,37] and TIPS-pentacene^[40] as active layer for X-ray direct photoconductor. The OSCs based direct X-ray detectors exhibit a real-time, fast ($<5 \text{ ms}$,^[38] see Figure 7a) box-shaped, response to the radiation, with a photocurrent amplitude linearly increasing with the impinging dose rate and a huge radiation hardness with stability of the signal after 2 kGy of total irradiation dose, as shown in Figure 7b.^[19] Interestingly, it has been found that the electrical transport properties of OSCs, and in particular their charge carrier mobility, do not represent a key parameter to reach high detection performance in OSC-based ionizing radiation detectors. In particular, Basiricò et al.^[20] compared the X-ray detection performance of rubrene-, characterized by a high conductivity and mobility ($\mu \approx 8 \text{ cm}^2 \text{ V}^{-1} \text{ s}^{-1}$), with those of DNN-based devices, having two orders of magnitude lower mobility ($\mu \approx 2 \times 10^{-3} \text{ cm}^2 \text{ V}^{-1} \text{ s}^{-1}$). Rubrene-based detectors showed lower sensitivity values, poorer photocurrent amplitude, and stability and a slower response dynamic with respect to DNN-based ones. These results are in good agreement with those reported for 4HCB SCs-based X-ray detectors.^[37]

Indeed, 4HCB can be grown in platelet shape, allowing the measure of the X-rays induced photocurrent along the three crystallographic axes. In this case, the lower mobility axis ($\mu < 1 \times 10^{-4} \text{ cm}^2 \text{ V}^{-1} \text{ s}^{-1}$) has been demonstrated as the one providing the higher photocurrent and sensitivity, confirming the previous study on Rubrene. The highest sensitivity value reported so far for an OSCs-based X-ray direct detector is $11.7 \mu\text{C Gy}^{-1} \text{ cm}^{-2}$

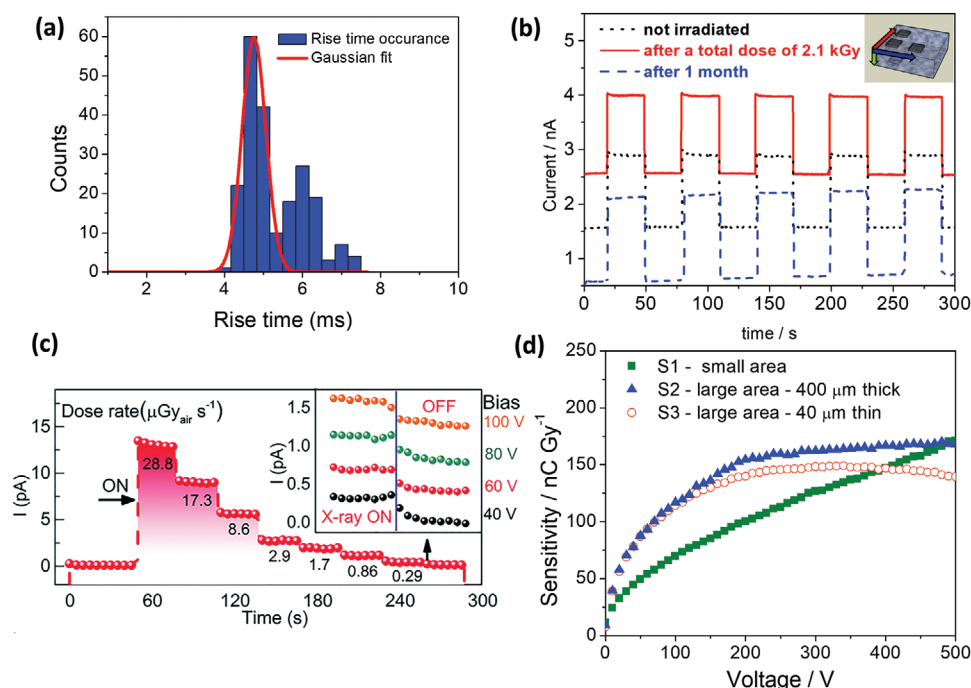


Figure 7. a) Histogram of the occurrences for rise times, showing the mean value at 5 ms, in the response of 4HCB-based detectors to synchrotron monochromatic beam with energy 10 keV, dose rate 40 mGy s^{-1} , and 20 V applied bias. Reproduced with permission.^[38] Copyright 2015, Wiley-VCH. b) Dynamic response to an on-off switching X-ray beam ($35 \text{ keV @ } 150 \text{ mGy s}^{-1}$), recorded along the c axis (i.e., low mobility axis, see inset) of a 4HCB SC-based detector, before (black dotted line) and after (red solid line) a total dose of 2.1 kGy; the blue dashed line indicates the same measure repeated after one month. Reproduced with permission.^[37] Copyright 2014, The Royal Society of Chemistry. c) Dynamic response to X-rays with changing dose rates at an electrical field of 0.6 kV cm^{-1} , showing the lowest detectable dose rate at $0.29 \mu\text{Gy s}^{-1}$; the inset shows the response curves at $0.29 \mu\text{Gy s}^{-1}$ under different bias voltages. Reproduced with permission.^[18] Copyright 2020, The Royal Society of Chemistry. d) Sensitivity of 4HCB SCs-based X-ray detectors as a function of applied bias, for a small area and $400 \mu\text{m}$ thick sample (green squares), for a large area, and $400 \mu\text{m}$ thick sample (blue solid triangles), and for a large area and $40 \mu\text{m}$ thin sample (red open triangles). Reproduced with permission.^[38] Copyright 2015, Wiley-VCH.

($1.75 \times 10^{-1} \mu\text{C Gy}^{-1} \text{cm}^{-3}$) at 500V for 400 μm thick 4HCB-based device. Actually, solution-grown cm-sized Rubrene SCs have been demonstrated to efficiently detect alpha particles from a ^{210}Po source (5.3 MeV) with an activity of $>500 \mu\text{Ci}$.^[41] The authors also gave a preliminary assessment of neutron detection with a ^{252}Cf source (0.9 MeV average energy), giving a further proof of the potentiality of Rubrene SCs for ionizing radiation detection.

Very recently Zhao et al.^[18] reported a sensitivity to X-rays of $10 \mu\text{C Gy}^{-1} \text{cm}^{-2}$ ($5 \times 10^{-1} \mu\text{C Gy}^{-1} \text{cm}^{-3}$) at 100 V for a 1mm thick 4HCB-based device, together with a record detection limit as low as $2.9 \times 10^{-1} \mu\text{Gy s}^{-1}$, the lowest value reported for OSCs-detectors (Figure 7c) and $\mu\text{-}\tau$ product of $8.5 \times 10^{-5} \text{cm}^2 \text{V}^{-1}$. Despite these results are referred to thick crystals, with rigid mechanical properties and requiring high operative voltage ($>100 \text{V}$), it is worth noting that maximizing the electrode/semiconductor interface active area, for example with the employment of larger electrode areas or interdigitated electrodes, the charge collection efficiency can be greatly improved (from 5% to 20% for a 4HCB crystal) and this allows to strongly decrease the operative bias voltage down to few Volts.^[38] Such behavior is shown in Figure 7d, where the sensitivity of 4HCB SCs-based detectors with different thicknesses and active areas are reported as a function of applied bias. From the plot it can

be also noticed that, following this approach, also the thickness of the OSCs can be decreased to few microns without losing in detection performance. The bendability of such system has been assessed,^[38] together with the possibility of fabrication through scalable printing technique (i.e., inkjet printing^[40]), paving the way to the development of novel large-area, flexible, and low-power consuming ionizing radiation sensors based on OSCs.

5.1.2. Perovskite Single Crystals

The first report proposing a PSC as active layer for direct X-ray detectors has been published in 2013. In this work Stoumpos et al.^[33] envisaged the employment for high-energy radiation detection of CsPbBr_3 single crystals grown by vertical Bridgman method using a three zone furnace, due to the high $\mu\tau$ product measured for electrons, $1.7 \times 10^{-3} \text{cm}^2 \text{V}^{-1}$, comparable to cadmium zinc telluride (CZT), and that for holes, that is, $1.3 \times 10^{-3} \text{cm}^2 \text{V}^{-1}$, 10 times higher than CZT. However, the actual real-time response to X-rays of a PSC-based detector was demonstrated only in 2016 by Wei et al.,^[49] who reported a detector made of 150 μm –3 mm thick MAPbBr_3 SC with photodiode configuration, exhibiting a record-high $\mu\tau$ product of

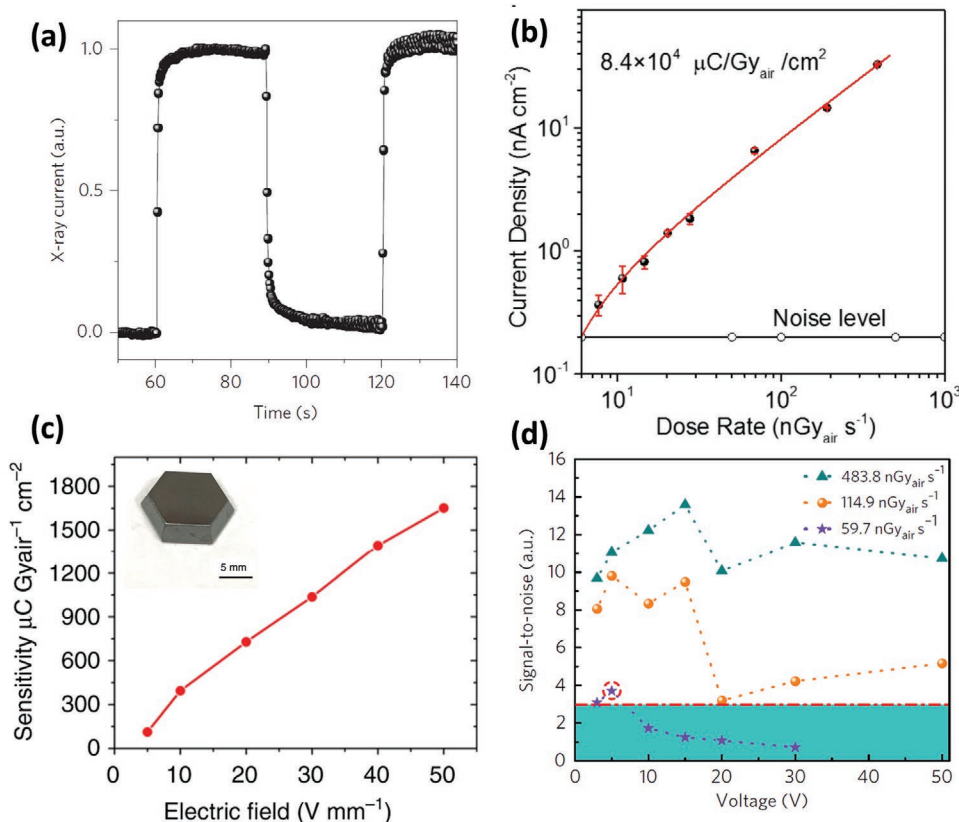


Figure 8. Perovskite Single Crystal-based X-ray detectors: a) Dynamic response of a MAPbBr_3 -based detector to X-rays from a Ag-targeted tube at 50 kVp, turned on and off. Reproduced with permission.^[49] Copyright 2016, Springer Nature. b) Current density output of 1 mm thick $\text{CH}_3\text{NH}_3\text{PbBr}_{2.94}\text{Cl}_{0.06}$ SC-based detector exposed to 8 keV X-rays at different dose rates. A sensitivity of $8.4 \times 10^4 \mu\text{C Gy}^{-1} \text{cm}^{-2}$ was calculated from the slope of the fitting line. Reproduced with permission.^[51] Copyright 2017, Springer Nature. c) Sensitivity at different electric fields for a $\text{Cs}_3\text{Bi}_2\text{I}_9$ SC-based X-ray detector (picture in the inset, the scale bar is 5 mm). Reproduced with permission.^[92] Copyright 2020, Springer Nature. d) Signal-to-noise ratio of a $\text{Cs}_2\text{AgBiBr}_6$ SC-based detectors. The red dashed line represents a SNR of 3, corresponding to a detection limit of $0.0597 \mu\text{Gy s}^{-1}$ at 5 V bias, indicated by the purple star surrounded by the red dashed circle. Reproduced with permission.^[53] Copyright 2017, Springer Nature.

$1.2 \times 10^{-2} \text{ cm}^2 \text{ V}^{-1}$ and sensitivity up to $80 \mu\text{C Gy}^{-1} \text{ cm}^{-2}$. The dynamic response of such detector to an X-rays from an Ag-targeted tube at 50 kVp, turned on and off is shown in Figure 8a. In the following years different kinds of PSCs, that is, hybrid^[47,50,51,87–89] and inorganic^[52] lead-halide, lead-free^[67,90–93] perovskites have been demonstrated as active layer for X- and γ -rays and α -particles detectors. The top X-ray detection performance reported so far for a PSCs-based device was reported by Wei et al.,^[51] who demonstrated that a Cl^- dopant compensation of p-type MAPbBr_3 SC results in a significant improvement of both bulk resistivity and hole mobility, enhancing thus the charge collection efficiency maintaining low dark currents. Such dopant-compensated $\text{MAPbBr}_{2.94}\text{Cl}_{0.06}$ SC-based detectors achieved sensitivity up to $8.4 \times 10^4 \mu\text{C Gy}^{-1} \text{ cm}^{-2}$ (Figure 8b) and LoD as low as $7.9 \times 10^{-3} \mu\text{C Gy}^{-1}$ for soft 8 keV X-ray detection.

Despite these excellent performances, one of the main concerns about the actual exploitation of lead-halide perovskite in electronic devices is their toxicity and environmental impact, which limit their employment in several fields of application such as medical dosimetry and diagnostics. To overcome this issue, in the very last years the first studies on lead-free PSCs as ionizing radiation detectors have been reported, employing bismuth as high-Z atom able to absorb the high energy photons.^[44,53,92] Zhang et al.^[92] reported on cm-sized $\text{Cs}_3\text{Bi}_2\text{I}_9$ SC-based X-ray detectors (Figure 8c), with a sensitivity up to $1.65 \times 10^3 \mu\text{C Gy}^{-1} \text{ cm}^{-2}$ and a LoD down to $1.3 \times 10^{-1} \mu\text{Gy s}^{-1}$ at 60 V, values in line with those reported for most of their inorganic lead-halide counterparts. A previous work on lead-free $\text{Cs}_2\text{AgBiBr}_6$ ^[53] SC-based detectors reported about one order of magnitude lower sensitivity at 50 V but with a lower LoD, that is, $5.97 \times 10^{-2} \mu\text{Gy s}^{-1}$ at 5V (Figure 8d).

Figure 9a,b summarize the top sensitivity and LoD values reported so far for OSCs- and PSCs-based X-rays detectors implemented with different material formulation. As expected, OSCs exhibit a much lower sensitivity than PSCs, because of the much lower radiation attenuation fraction due to their low-Z. On the other hand, the LoD values of the two classes of materials are comparable, thanks to the good stability and low achievable dark currents that characterize both classes of materials.

The values reported in Figure 9 refer to very different device structures and experimental conditions, such as operative bias

and energy of the X-rays sources. In Table 1 for OSCs and Table 2 for PSCs more information are reported for a detailed comparison.

5.2. Thick/Thin Film Detectors

5.2.1. Organic Films

Organic films were at first investigated for X-ray detection, as the film structure fully benefits from the solution-based deposition techniques, that is, fast and easy coverage of large areas with low costs, low-temperature procedures that allow deposition over thin plastic substrates, envisaging thus flexible-electronics application.

Since 2007 Prof. Sellin and collaborators began to study conjugated polymer as direct x-ray organic detectors. The first works employed photodiode devices based on spin coated thick films of 5–30 μm of large bandgap semiconductor polymers, such as poly[1-methoxy-4-(2-ethylhexyloxy)-phenylenevinylene] (MEH-PPV),^[56] poly(9,9-dicytluorene) (PFO),^[56] and PTAA.^[54,94] Despite achieving moderate performances, these preliminary works paved the way for highly sensitive organic/hybrid direct X-ray detectors reported in the following years.

Efficient detection of high-energy photons by organic semiconductors requires to maximize the interaction of the active absorbing organic layer with the radiation, which can be achieved by enhancing the Z of the semiconductor and/or by increasing the interaction volume, that is, the film thickness.

Alternatively, the amplification of X-ray induced photocurrent by gain effect can be exploited to maintain tissue-equivalent, thin, flexible systems. The efficacy of this approach has been assessed by full-organic (TIPS-pentacene based) thin film X-ray detectors, in photoconductor^[21] and phototransistor^[73] architectures, showing the possibility of combining high detection performance at ultra-low bias voltage (<1 V) with flexible mechanical properties, and demonstrating the reliability for security^[95] and medical applications.^[30] Figure 10a shows the typical X-ray induced photocurrent dynamics (upon three on/off switching cycles of the X-ray beam) in organic thin film-based detectors.

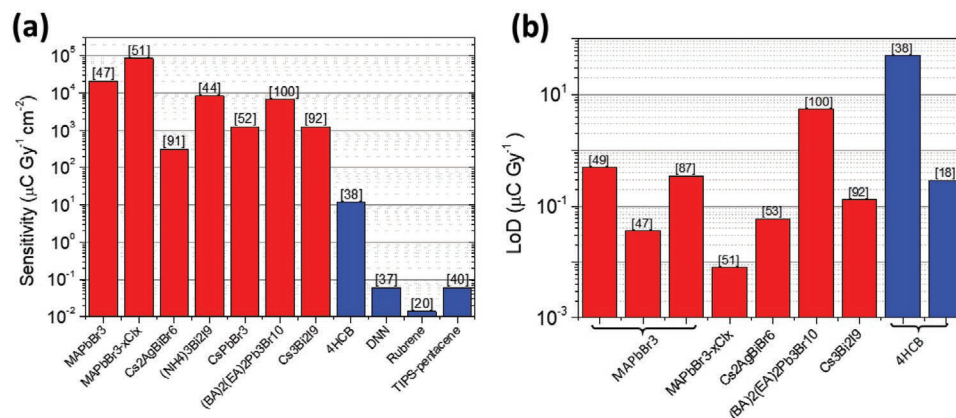


Figure 9. Comparison of top sensitivity and LoD values for organic and perovskite-based detectors: Histograms of the a) top sensitivity and b) LoD of different materials reported for OSCs- (blue) and PSCs- (red) based X-ray detectors.

Table 1. Organic single crystals. Slow solvent evaporation (SSE), physical vapor deposition (PVD).

Material	Growth method	Structure	Thickness	Active area	V_{Bias}	I_{dark}	S_A [$\mu\text{C Gy}^{-1} \text{cm}^{-2}$]	LoD [$\mu\text{Gy}_{\text{air}} \text{s}^{-1}$]	Response time	Radiation source
4HCB ^[19] NTI ^[19]	SSE	Photoconductor (Au,Ag)/OSC/(Au,Ag) PEDOT/OSC/PEDOT	600 μm	16 mm^2	50–500 V	6 nA 2 nA	0.3 ^{a)}	NA	<70 ms	Mo target, 35 kVp (peak@17 keV)
4HCB ^[37]	SSE	Photoconductor Ag/OSC/Ag	up to mm	mm^2	10–100 V	1 nA	0.7 ^{a)}	NA	NA	Mo target, 35 kVp (peak@17 keV)
DNN ^[37]	SSE	Photoconductor Ag/OSC/Ag	up to mm	mm^2	1–10 V	0.1 nA	0.061 ^{a)}	NA	NA	Mo target, 35 kVp (peak@17 keV)
DNN ^[20]	SSE	Photoconductor metal/OSC/metal	200 μm	mm^2	5 V	0.1 nA	0.033 ^{a)}	NA	<100 ms	Mo target, 35 kVp (peak@17 keV)
Rubrene ^[20]	PVD ^{b)}	Photoconductor metal/OSC/metal	NA	mm^2	5 V	4–0.08 nA	0.014 ^{a)}	NA	>10 s	Mo target, 35 kVp (peak@17 keV)
Rubrene ^[41]	SSE and PVD ^{b)}	Photoconductor graphite/PEDOT /OSC/ PEDOT /graphite	1–2 mm	1.4 cm length	3000 V cm^{-1}	NA	NA	NA	NA	γ -rays ²¹⁰ Po (α , 5.3 MeV) ²⁵² Cf (n, 0.9 MeV)
4HCB ^[38]	SSE	Photoconductor (Au, Ag, graphite)/OSC/ (Au,Ag, graphite)	40–400 μm	0.15–2 mm^2	5–500 V	6–600 nA cm^{-2}	11.7 ^{a)}	50	<5 ms	Mo-target, 35 kVp (peak@17 keV) Synchrotron radiation (8.3–25 keV)
4HCB ^[39]	SSE	Photoconductor Au/OSC/Au	200 μm	2–4 mm^2	100–800 V	0.6–9.6 nA cm^{-2}	NA	NA	70 $\mu\text{s}^{\text{c)}}$	²⁴¹ Am (α , 5.49 MeV)
TIPS- pentacene ^[40]	Inkjet printing	Photoconductor Au/OSC/Au	8.1 μm	1.3 $\text{mm}^{2\text{a)}$	1 V	\approx 2 nA	0.058 ^{a)}	NA	>10 s	Mo-target, 35 kVp (peak@17keV)
4HCB ^[18]	SSE	Photoconductor Au/OSC/Au	1 mm	5 mm^2 (X) 7 mm^2 (α)	40–100 V	0.1 pA	10	0.29	5–12 $\mu\text{s}^{\text{c)}}$	W-target, 50 kVp ²⁴¹ Am (α , 5.49 MeV)

^{a)}not reported by the authors, estimation based on published data; ^{b)}no solution grown method; ^{c)}pulse from α -particle.

Blends of organic semiconductors with nanocomposites have been proposed as a technological strategy to enhance the X-ray attenuation efficiency of organic materials, allowing to increase the layer thickness, and maintaining in the meantime the advantages of solution processes. With this aim Intaniwet et al.^[96] proposed a blend of high-Z bismuth oxide (Bi_2O_3) nanoparticles (NPs) ($Z = 83$ for Bi) and PTAA 20 μm thick film as active layer of a X-ray direct detector in photodiode architecture. The authors obtained an enhancement in sensitivity by 2.5 times, from 78 $\mu\text{C Gy}^{-1} \text{cm}^{-3}$ in the PTAA detector to $2 \times 10^2 \mu\text{C Gy}^{-1} \text{cm}^{-3}$ in the blended device when operated at -200 V. In a following publication, the authors investigated the role of the electrical properties of the NPs on the detection performance, by comparing the effects of metallic Ta NPs and insulating Bi_2O_3 NPs in blend with PTAA and poly([9,9-dioctylfluorenyl-2,7-diyl]-co-bithiophene) (F8T2), forming a 5 μm thick active layer of a photodiode structure. Interestingly, they observed that, despite the higher molecular mass therefore higher attenuation of Bi_2O_3 , the X-ray induced photocurrent and the sensitivity of the Ta-loaded photodiode is higher ($4.34 \times 10^2 \mu\text{C Gy}^{-1} \text{cm}^{-3}$ corresponding to $2.17 \times 10^{-1} \mu\text{C Gy}^{-1} \text{cm}^{-2}$) than those of the Bi_2O_3 -loaded photodiodes (see Figure 10b). The authors hypothesize that the higher conductivity of metallic Ta NPs induces a more efficient charge transfer to the polymeric matrix, leading to the higher X-ray detection performance observed. However, the electrical and detection performances reported for these devices are poor, with

small photocurrent at high operative reverse bias in 50–200 V range. These works bring to light the major challenge of this approach: the heavy nanoparticles are not uniformly distributed in the organic matrix, but they form aggregates that are detrimental for electrical performance of the device.

Ciavatti et al.^[25] demonstrated how the combination of two effects, that is, enhancement of radiation attenuation through high-Z absorbers and photoconductive gain can be exploited to achieve higher X-ray sensitivity. With the aim to study the role of electrode-semiconductor interface barriers and the impact of heavy NP-loading to the X-ray detection performance in such hybrid organic/inorganic direct detectors, the authors fabricated organic photodiodes with a very efficient rectification ratio doped with high-Z Bi_2O_3 NPs and compared the X-ray response of the detector in charge-injection conditions (forward bias) and in charge-collection conditions (reverse bias). For NP-free polymer photodiodes operating in reverse bias (-80 V), the devices reach sensitivity up to 24 $\mu\text{C Gy}^{-1} \text{cm}^{-2}$, with a fast (<10 ms), box-shaped photoresponse. On the other hand, in forward operation, a slower kinetics has been observed but with a sensitivity two orders of magnitude higher than in reverse bias. This effect has been attributed to the activation of a photoconductive gain effect, due to the high-injection condition. Adding Bi_2O_3 NPs to the organic semiconductor layer results in different effects for the two operation regimes: in reverse operation, the photocurrent is increased up to a 5 wt% NPs loading. In forward regime, no improvement

Table 2. Perovskite single crystals. Antisolvent vapor-assisted crystallization (AVS), inverse temperature crystallization (ITC).

Material	Growth method	Structure	Thickness	Active area	V_{Bias}	I_{dark}	S_A [$\mu\text{C Gy}_{\text{air}}^{-1} \text{cm}^{-2}$]	LoD [$\mu\text{Gy}_{\text{air}} \text{s}^{-1}$]	Response time (Cut-off freq)	X-ray source
CsPbBr_3 ^[33]	Bridgman ^{b)}	Photoconductor Ag/PSC/Ag	2.1 mm	\varnothing 7 mm	450 V	NA	NA	NA	NA	Ag-target, 40 kVp
MAPbBr_3 ^[49]	AVC	Photodiode Au/PSC/BCP/Au	2–3 mm	4–16 mm ²	–0.1 V	29 nA cm ^{–2}	80	0.5	730 μs (480 Hz)	Ag target, 50 kVp
MAPbI_3 , MAPbBr_3 , MAPbCl_3 , FAPbI_3 , FAPbBr_3 and I-treated MAPbBr_3 ^[50]	ITC	Photoconductor Ag/PSC/Ag	\approx 2 mm	8 mm ²	4–10 V	\approx 2 nA	650	NA	(200 Hz)	Cu-target, and γ -ray ¹¹ C (0.96 MeV) ¹³⁷ Cs (0.662 keV) ¹⁸ F (511 keV) ²⁴¹ Am (596 keV)
MAPbBr_3 ^[47]	Modified ITC-integrated on Si wafer	Photodiode Au/BCP/Per SC/Si	2 mm	0.044 mm ²	–7 V	NA	2.1×10^4 (150 μm thick)	0.036 (2 mm thick)	NA	Cu-target
$\text{MAPbBr}_{3-x}\text{Cl}_x$ ^[51]	AVC and ITC	photodiode	2–5.8 mm	1 cm ²	–5 V	NA	8.4×10^4	0.008	NA	Cu-target
$\text{Cs}_2\text{AgBiBr}_6$ ^[53]	Modified ITC	Photoconductor Au/PSC/Au	2 mm	3.14 mm ²	50 V	NA	105	0.0597	NA	W-target, 50 kVp
MAPbBr_3 ^[87]	Variable temperature crystallization	p-i-n photodiode	2–7 mm	250 μm	–100 V	20 nA cm ^{–2}	2.36×10^4	0.35	26 μs	X-ray 30 kVp
$\text{Cs}_2\text{AgBiBr}_6$ ^[91]		Photoconductor Au/PSC/Au	2 mm	\approx 4mm ²	100 V (50 V mm ^{–1})	NA	316 (RT) 988 (77K)	NA	NA	W-target, 50 kVp
CsPbBr_3 ^[99]	Bridgman ^{b)}	Photoconductor Au/PSC/Au photodiode Ga/PSC/Au	up to 3 mm	\approx 1 cm ²	NA, –150 V	10nA (83.3 nA cm ^{–2})	NA	NA	NA	γ -ray ⁵⁷ Co (122 keV) ¹³⁷ Cs (662 keV)
2D layered (NH_4) ₃ Bi ₂ I ₉ ^[44]	Low-temperature solution	Photoconductor	7 mm	21 \times 20 mm ²	1–10 V	NA	803 (–) 8.2×10^3 (//)	0.055 (–) 204 (//)	NA	Ag-target, 50 kVp (Amptek Mini-X)
CsPbBr_3 ^[52]	improved low temperature solution	Photodiode	2–3 mm	3.14 mm ²	40 V	3nA	1256	NA	NA	W-target, 80 kVp ²⁴¹ Am (α , 5.5 MeV)
2D trilayer (BA) ₂ (EA) ₂ Pb ₃ Br ₁₀ ^[100]	Slow cooling from aqueous acid solution	Photoconductor Au/PSC/Au	2 mm	10 mm ²	10 V	7 nA cm ^{–2}	6.8×10^3	5.5	NA	W-target, 70 kVp
$\text{Cs}_3\text{Bi}_2\text{I}_9$ ^[92]			1.2 mm	1 mm ²	50 V mm ^{–1}	NA	1652.3	0.13	NA	W-target, 40 kVp

^{a)}not reported by the authors, estimation based on published data; ^{b)}no solution grown.

is observed as the conductive gain effect breaks down due to the NPs surface agglomeration and weakened charge injection.

In 2016, a similar approach was also reported by Anka et al.,^[26] which presented an hybrid–organic direct X-ray photodetector fabricated using inorganic lead sulfide (PbS) nanocrystal quantum dots blended in a semiconducting polymer matrix, constituted by a P3HT:PCBM bulk heterojunction (BHJ). Quantum dots acts as absorbing centers and directly convert X-rays into charge-carriers that are then transported through the organic BHJ to the electrodes.

More recently, a similar BHJ photodiode X-ray detector structure has been reported, with a 10–30 μm thick active layer made of organic P3HT:PCBM BHJ blended with Bi₂O₃ NPs instead of PbS to reduce the environmental impact.^[23] The nanoscale diodes near the NPs, within the whole BHJ volume, should lead to an in-built depletion region, allowing efficient charge-

collection detection process. However, the authors suggests that, even at a high reverse bias (–10 V) with a charge collection efficiency estimated exceeding the 60%, a photoconductive gain occurs with increasing of NPs concentration (Figure 10c), probably due to the low rectification of the diode, as witnessed by the high dark current measured, in the range 10^{-4} – 10^{-6} A cm^{–2}. This mixed behavior would explain the high sensitivity measured, that is, 1.7×10^6 $\mu\text{C Gy}^{-1} \text{cm}^{-3}$ corresponding to 3.9×10^3 $\mu\text{C Gy}^{-1} \text{cm}^{-2}$ and the slow component of the signal observed (rising time >100 ms) (Figure 10d).

A different strategy by Büchele et al.^[60] is worth mentioning, even if not involving a strictly direct detection of X-rays. They reported on X-rays photodiodes with an active layer based on scintillating terbium-doped gadolinium oxysulfide (GOS:Tb) X-ray absorbers blended in a polymer BHJ (P3HT:PCBM), resulting in a quasi-direct X-ray detector with a sensitivity up

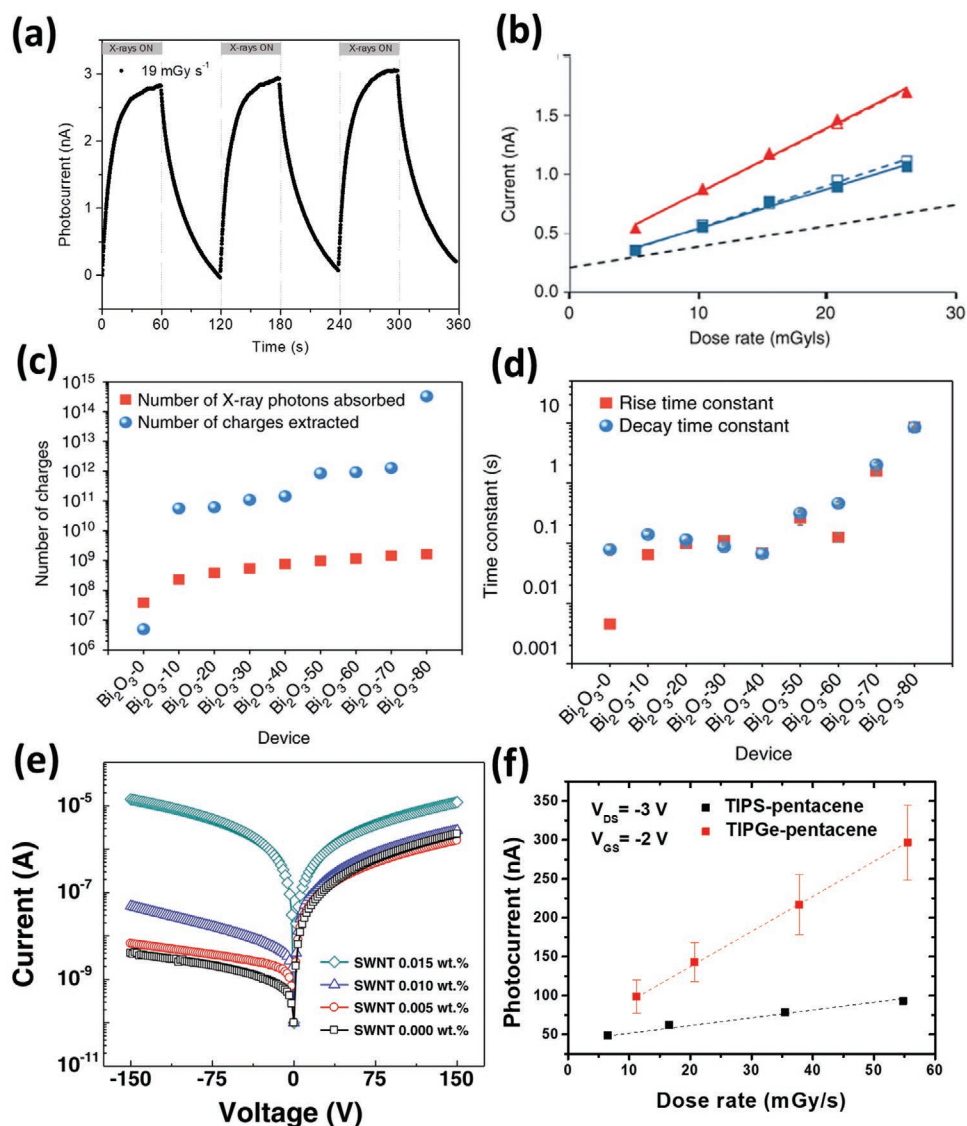


Figure 10. Organic film-based X-ray detectors: a) X-ray-induced photocurrent from an organic thin-film X-ray photoconductor biased at 0–2 V upon three on/off switching cycles of a monochromatic synchrotron X-ray beam at 17 keV. Reproduced with permission.^[21] Copyright 2016, Springer Nature. b) Plot of the photocurrent in function of the X-rays dose rate for a ITO/F8T2 (NP)/Au (solid symbols) and ITO/F8T2 (NP)/Al (open symbols) diodes, loaded with 30 wt.% Bi₂O₃ (triangles) and 30 wt.% Ta (squares) NPs in 5 μm thick films, irradiated with 17.5 keV X-rays. The dashed line indicates the induced photocurrent produced in a NP-free device. Reproduced with permission.^[24] Copyright 2013, IOP Publishing Ltd. Comparison between number of X-ray photons absorbed by each device and the number of c) charges extracted and the d) rise and decay times at different NPs concentrations for a BJT:NPs blended photodiode. The increase of extracted charges and the response times with the NPs loading indicates the occurring photoconductive gain effect. Reproduced with permission.^[23] Copyright 2018, Springer Nature. e) Dark current-voltage characteristics of X-rays photodiode based on polymer blended with carbon nanotubes. The diode loses its rectifying behavior with the increase of carbon nanotubes concentration. Reproduced with permission.^[97] Copyright 2014, Springer Nature. f) Comparison between X-rays induced photocurrent at different dose rates for TIPS-pentacene (black squares) and TIPGe-pentacene (red squares) X-ray phototransistors. Reproduced with permission.^[28] Copyright 2018, Wiley-VCH.

to 459 e⁻ nGy⁻¹ mm⁻² (corresponding to 7.34 μC Gy⁻¹ cm⁻²) at -10V.

As a general comment, although improvement in the detecting performance has been demonstrated, all of the organic/nanocomposites blends are intrinsically limited by critical value of NPs/QDs concentration in the blend, above which clustering and agglomeration occur, resulting in the degradation of electronic transport properties of the active layer. Moreover, the employment of thick films to increase the X-rays

absorption, results in an increase of the operating voltage and limits the bendability of the device, thus sacrificing the potential advantages for flexible and wearable sensors. A further important limitation of such approach is the loss of the tissue equivalence, which is a unique peculiarity of organic materials for ionizing radiation detection that opens important pathways for medical dosimetry application.

To overcome this loss an alternative approach is constituted by blending the organic active layer with other organic

compounds to improve the charge transport properties of the device and its efficiency as X-ray detector by consequence.

The first attempt in this direction was made in 2011 by Intaniwet et al.,^[55] who reported on a blend of poly(triarylamine) (PTAA) and TIPS-pentacene in the active layer of a photodiode structure. The aim was to improve the transport of holes thanks to the high mobility of the TIPS-pentacene molecule, however moderate sensitivity has been reached at 100 V with 10 μm thick device. Also, some trials by blending in a polymer matrix carbon nanotubes have been made, improving the detector sensitivity and preserving the tissue equivalence but still having the issue of agglomeration and clustering as shown in Figure 10e.^[97]

Very recently, Temiño et al.^[22] reported on a highly sensitive X-ray detector based on a full-organic thin film blend of TIPS-pentacene and Polystyrene (PS) in phototransistor architecture. The authors demonstrate that charge mobility and thin-film morphology (i.e., number and size of grain boundaries) are the two main parameters affecting the photoconductive gain process and the carrier trapping effects, that is, the physical phenomena ruling the direct detection of high-energy radiation by organic films. The addition of PS results in the passivation of the hydroxyl groups of SiO₂ dielectric employed, enhancing thus the hole mobility of the semiconductor. The use of the BAMS technique allowed to control the grain boundary density and to achieve a low minimum detectable dose rate of 35 μGy s⁻¹ and a record sensitivity of 1.3 × 10⁴ μC Gy⁻¹ cm⁻², the highest reported for organic-based detector.

A different and innovative strategy recently reported to improve the X-ray detection performance of thin film-based fully-organic devices is based on the chemical synthesis of novel organic semiconducting small molecules tailoring their transport and absorption properties.^[28] In particular, new solution-processable organic molecules derived from

TIPS-pentacene and 2,8-difluoro-5,11-bis(triethylsilylethynyl) anthradithiophene (diF-TES), with Ge-substitution in place of the Si atoms to increase the material atomic number, and having a higher mobility of their Si-counterparts, were demonstrated to boost the X-ray detection performance of organic thin film-based detectors in phototransistor configuration (Figure 10f).

5.2.2. Perovskite Films

Despite the first report on Perovskite film-based X-ray detector was published by Yakunin et al.^[16] in 2015, only in the last couple of years this class of devices gained the interest of the research community. Most recent works on perovskite detectors focused on finding technological strategies to enhance the film thickness, that is, the radiation absorption, maintaining a high μτ to guarantee high charge collection efficiency. For this reason, often pressing and melting processes have been employed for fabrication^[66–69] and the highest sensitivity for perovskite film detectors has been reported by Hu et al.,^[68] who measured a sensitivity of 1.22 × 10⁵ μC Gy⁻¹ cm⁻² for a 800 μm thick MAPbI₃ wafer grown by a heating-assisted press method.

However, Kim et al.^[61] demonstrated highly efficient large-area 830 μm thick MAPbI₃ X-ray detector fabricated by means of solution-growth techniques. The authors conceived an innovative all-solution based method to synthesize perovskite polycrystalline

thick film composed by 20–100 μm sized crystallites, allowing blade-coating printing onto large-area TFT backplane. On the bottom and on the top of the absorbing layer, two interlayers of polyimide-perovskite composites were inserted by spin-casting to reduce the dark current (structure reported in Figure 11a). The authors reported a large charge-carrier μτ product value (1.0 × 10⁻⁴ cm² V⁻¹), sensitivity up to 1.1 × 10⁴ μC Gy⁻¹ cm⁻² and assessed fast response to a train of short X-ray pulses with a pulse width of 50 ms, indicating low trap-density (Figure 11b).

The employment of thin films remains, however, the only possible way to envisage the implementation of flexible perovskite detectors. For this reason, many of the last published works investigate novel perovskite formulations,^[15] deposition techniques^[59,98] and architectures^[65] able to guarantee high detection performances even in thin film form. In 2019 Liu et al.^[64] reported the first flexible perovskite-based X-ray detectors. Their method involves inkjet printing of a CsPbBr₃ QDs-based solution onto metal electrodes pre-patterned on Si or flexible PET substrate, resulting in 20 nm thick perovskite layer in photoconductor architecture. The authors observed a highly reproducible fast response (about 30 ms of rise time) to the X-rays at bias voltages below 1 V (Figure 11c). The sensitivity value reached for flexible detectors, 177 μC Gy⁻¹ cm⁻² is about four times lower than that for rigid device (i.e., 83 μC Gy⁻¹ cm⁻²) under soft X-ray-near UV synchrotron beamline (100–2500) eV, biased at 0.1 V.

Finally, in a very recent publication Tsai et al.^[79] reported on the first 2D layered perovskite (BA)₂(MA)₂Pb₃I₁₀ (Pb₃) highly crystalline thin film as X-ray detector. The resulting device is a 600 nm p-i-n photodiode with a 470 nm thick active layer. Figure 11e reports the comparison between the current-density-voltage plot in dark and under 10.91 keV X-ray exposure, for the 2D Pb₃-detector and a reference Si-photodiode. The plot shows how the 2D PbBr₃-detector detection performances surpasses the Si-photodiode both in dark current and photocurrent amplitude, and a comparable signal-to-noise level and sensitivity to Si photodiode as shown in Figure 11f.

Figure 12 reports the histogram of the distribution of the top values of sensitivity per unit volume (Figure 12a) and sensitivity per unit area (Figure 12b) reported for different organic and perovskite compounds employed to realize thick/thin film-based X-ray detectors. These two graphs highlight the different results achievable for the two kinds of normalization. Generally speaking, the comparison of the sensitivity per unit area highlights the operative detector performance, whereas the sensitivity per unit volume highlights the material property. CsPbBr₃ QD^[64] and TIPS-pentacene:PS^[22] show the highest potential among the perovskite and organic/hybrid materials investigated, respectively. Noteworthy, these refer to the two thinnest active layers among those reported, leading to the high sensitivity per unit volume shown in Figure 12a. Looking at Figure 12b, the most sensitive device resulted MAPbI₃ wafer photoconductor reported by Hu et al.^[68] In Figure 12b is also reported the variation in thickness of the absorbing layer of the top sensitivity materials. A more complete overview is given in Figure 12c, reporting the sensitivity values per unit area as a function of the active layer thickness for all the thick/thin organic and perovskite-based direct X-ray detectors reported so far, to the best of our knowledge. The

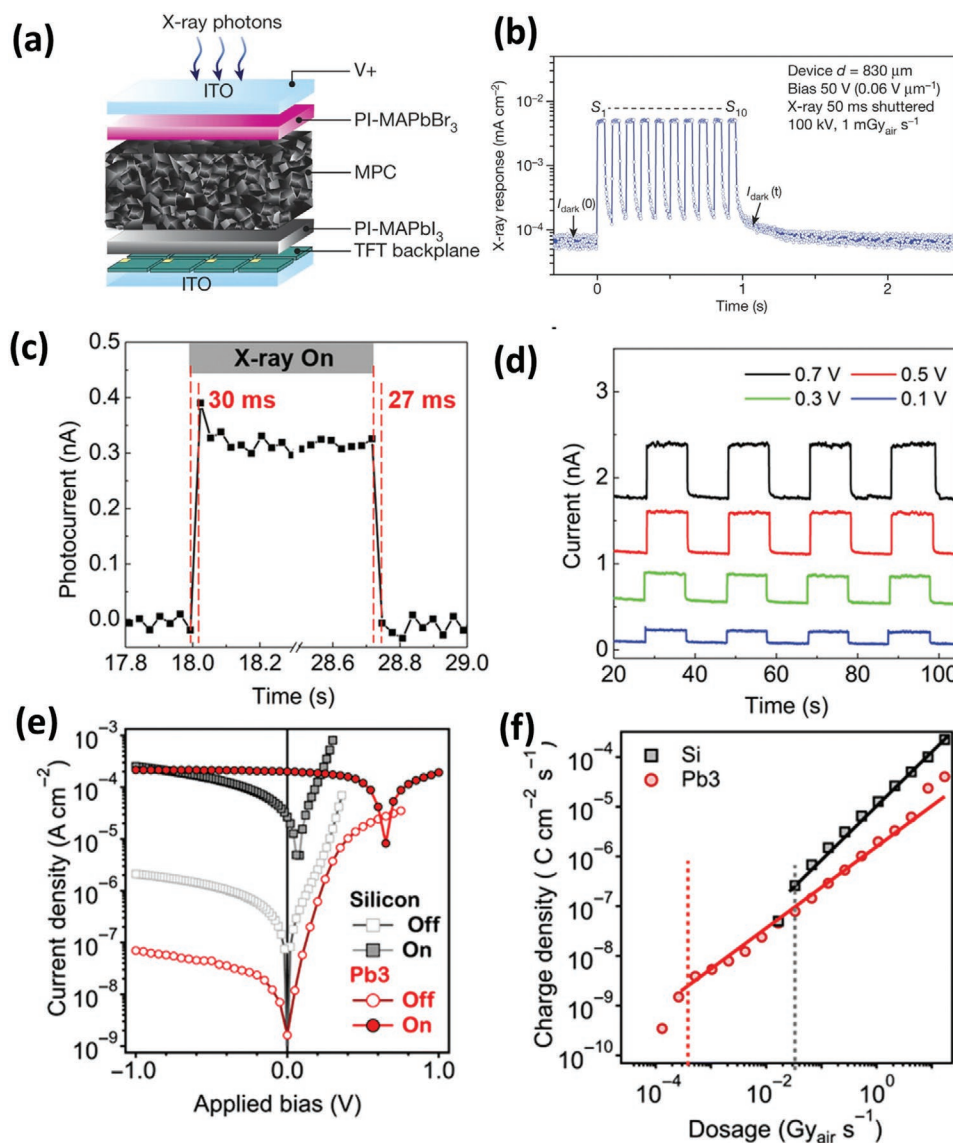


Figure 11. Perovskite film-based X-ray detectors: a) Structure of the all-solution-processed polycrystalline thick MAPbI₃ X-ray photoconductor. Reproduced with permission.^[61] Copyright 2017, Springer Nature. b) Dynamic response of printed MAPbI₃ polycrystalline thick film detector at 50 V to a train of short soft X-ray pulses with a pulse width 50 ms. Reproduced with permission.^[61] Copyright 2017, Springer Nature. c) Time response of CsPbBr₃ QDs-based photoconductor. Reproduced with permission.^[64] Copyright 2019, Wiley-VCH. d) Reproducibility of the dynamic response of the CsPbBr₃ QDs-based photoconductor for different biases below 1 V. Reproduced with permission.^[64] Copyright 2019, Wiley-VCH. e) Plots of current density versus voltage for 2D Pb₃-photodiode and silicon reference devices in the dark and under X-ray (10.91 keV) exposure. Reproduced with permission.^[79] Copyright 2020, American Association for the Advancement of Science. f) X-ray-induced charge density subtracted by the dark noise for 2D Pb₃-photodiode and silicon reference detector. Reproduced with permission.^[79] Copyright 2020, American Association for the Advancement of Science.

plot shows, at first approximation, a linear correlation between the sensitivity of perovskite detectors and the layer thickness (red dots), suggesting a relevant role of the increase of X-ray attenuated fraction. In the organic-based devices, instead, the sensitivity is much less correlated with thickness. The two thinnest detectors (few tens of nanometers), both for organic and perovskite, emerge as highly sensitive devices, indicating that in these cases, an efficient charge transport and high gain, occur. Finally, Figure 12d shows the histogram of the LoD for perovskite (red) and organic/hybrid (blue) materials as direct X-ray detectors: interestingly, the two classes of mate-

rials exhibit a behavior similar to the one observed for single crystals.

For a more exhaustive comparison the reader should refer to **Tables 3,4**, reporting details on thick/thin film organic and perovskite direct X-ray detectors, respectively.

6. Imaging Large-Area Detectors

This paragraph provides an overview on the tests reported to assess the applicability of organic and perovskite direct X-ray

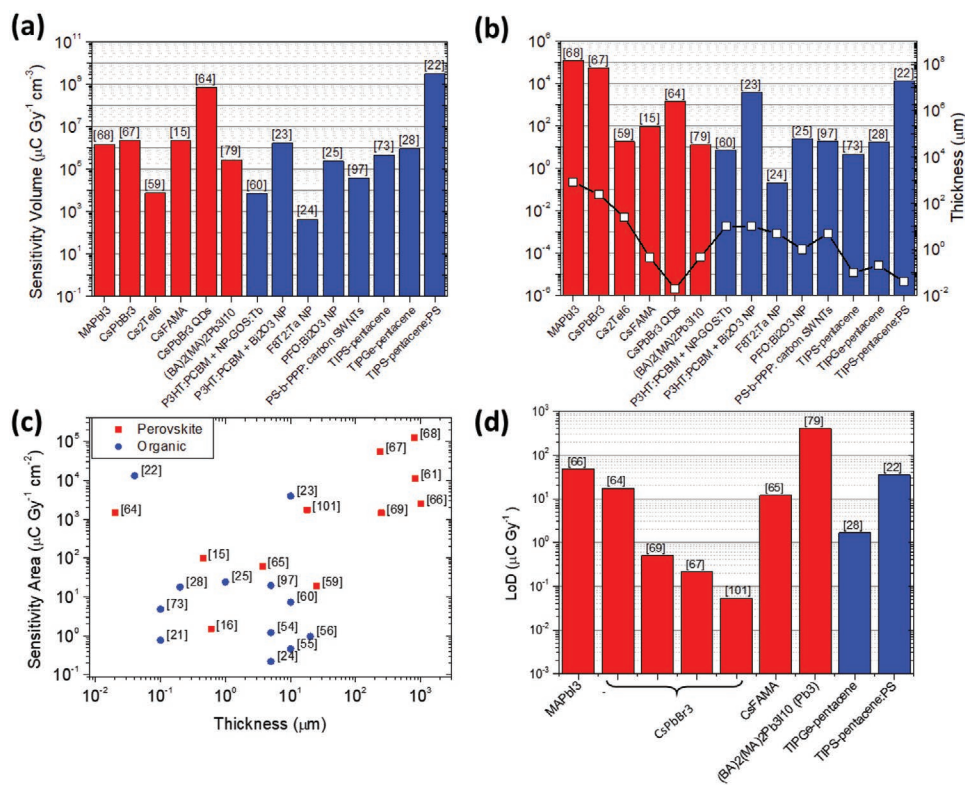


Figure 12. Comparison of top sensitivity and LoD values for organic- and perovskite-based X-ray detectors: Histogram of the top sensitivity values per a) unit volume and b) unit area for the materials reported as thick/thin active layer of perovskite (red) and organic/hybrid (blue) direct X-ray detectors. In (b) is also reported their variation in thickness (empty black squares—right axis). c) Plot of the sensitivity values in function of the active layer thickness for all the thick/thin X-ray detectors reported to the best of our knowledge. d) Histogram of the LoD for the reported perovskite (red) and organic/hybrid (blue) materials for direct X-ray detectors.

detectors for imaging application, envisaging the implementation of large area detecting systems for diagnostics and industrial inspection. **Figure 13** reports relevant examples for the different materials and structures discussed this review. Figure 13a reports X-ray imaging with a PSC detector based on a Si-integrated MAPbBr₃ crystal.^[47] The device consists of a ten pixels linear array (pixel size of 200 μm and pitch of 400 μm) fabricated onto the single crystal's top surface. Each pixel is connected by a single copper wire to a current amplifier and the bottom Si substrate acts as a common contact. A 10 mm-sized “N-shaped logo” is scanned twice linearly in one direction between the X-ray source and the detector, obtaining the X-ray image shown in Figure 13a, where each single copper cylinder forming the object can be clearly distinguished. A similar concept has been reported by Wang et al.,^[87] who developed a passive 40 \times 40 p-i-n array made of 7 mm thick MAPbBr₃ PSC with 250 μm width lines. In the bottom of Figure 13b the optical and X-ray image of a chicken claw are shown, obtained by a X–Y scanning of the detector. Figure 13c shows the X-ray image of a structured aluminum profile obtained by means of a full-organic TIPS-pentacene thin film flexible detector under a 17 keV monochromatic X-ray beam, provided by a synchrotron radiation beamline for medical physics diagnostic application.^[30] The image was also in this case recorded by a X–Y scanning of the detector. The same operation mode has been adopted by Yakunin et al.,^[16] reporting the X-ray image of a

Begonia obliqua L. leaf (Figure 13d), obtained by a 60 μm thick film MAPbI₃ photoconductor detector. Other researchers proposed imagers fabricated by interfacing the absorbing layer with a TFTs active matrix backplane. In the works of Jayawardena et al.^[70] and Kim et al.^[61] this approach has been followed for thick hybrid BHJ:NPs and MAPbI₃ films respectively. Figure 13e shows the schematic of the imager architecture and the modulation transfer function (MTF) (0.2 at $\approx 1 \text{ lp mm}^{-1}$) of the BHJ: NPs 250 μm thick active layer interfaced with an active matrix TFTs backplane. In Figure 13f the X-ray image and MTF (0.2 at 3.1 lp mm^{-1}), of a printed 830 μm thick MAPbI₃ photoconductor are reported.

These results, even if still preliminary, clearly indicate the large potential of organic- and perovskite-based detectors as large-area X-ray imagers.

7. Challenges and Outlook

The recent massive progress in the field of organic semiconductors and perovskites (both in terms of material technologies and device development) assessed their large potential for the implementation of innovative and unprecedented applications. Their use in the detection of ionizing radiation is compelling, as they can satisfy all the major X-ray detector requirements coupled to unique properties such as solution-processability,

Table 3. Organic/hybrid thick/thin films.

Material	Growth method	Structure	Thickness	Active area	V _{bias}	I _{dark}	S _A [μC Gy _{air} ⁻¹ cm ⁻²]	S _v [μC Gy _{air} ⁻¹ cm ⁻³]	LoD [μGy _{air} s ⁻¹]	Response time	X-ray Source
MEH-PPV ^[56]	Drop casting	Schottky diode ITO/PEDOT:PSS/polymer/Al	20 μm	5 × 5 mm ²	10 V (5 kV cm ⁻¹)	4 nA cm ⁻²	0.4 ^{b)}	200	NA	<150 ms	Mo-target, 50 kVp (peak at 17 keV)
PFO ^[56]	Drop casting	Schottky diode ITO/PEDOT:PSS/polymer/Al	20 μm	5 × 5 mm ²	50 V (25 kV cm ⁻¹)	4 nA cm ⁻²	0.96 ^{b)}	480	NA	<150 ms	Mo-target, 50 kVp (peak at 17 keV)
PTAA ^[54]	Spin-coating	Photodiode ITO/PEDOT:PSS/PTAA/metal	5 μm	0.5 × 0.5 cm ²	300 V	3.2 nA	1.2 ^{a)}	2.4 × 10 ^{3a)}	NA	<250 ms	Mo-target, 50 kVp (peak at 17 keV)
PTAA:TIPS-pentacene ^[55]	Spin-coating	Photodiode ITO/PTAA:TIPS/Al	10 μm	0.6 nA cm ⁻²	100 V	0.6 nA cm ⁻²	0.457 ^{a)}	457	NA	<250 ms	Mo-target, 50 kVp (peak at 17 keV)
PTAA:Bi ₂ O ₃ NPs ^[96]	Spin-coating	Photodiode ITO/PTAA:Bi ₂ O ₃ NP/Al	20 μm	0.25 cm ²	-200 V	0.25–0.9 nA cm ⁻²	0.4 ^{b)}	200	NA	NA	Mo-target, 50 kVp (peak at 17 keV)
F8T2:Ta NPs ^[24]	Spin-coating	Photodiode ITO/blend/metal (Au,Al)	5–20 μm	0.25 cm ²	50 V	0.7–0.02 nA	0.217 ^{a)}	434	NA	NA	Mo-target, 50 kVp (peak at 17 keV)
F8T2:Bi ₂ O ₃ NPs ^[24]	Spin-coating	Photodiode ITO/blend/metal (Au,Al)	5–20 μm	0.25 cm ²	50 V	0.7–0.02 nA	0.217 ^{a)}	377	NA	NA	Mo-target, 50 kVp (peak at 17 keV)
PTAA:Bi ₂ O ₃ NPs ^[24]	Spin-coating	Photodiode ITO/blend/metal (Au,Al)	5–20 μm	0.25 cm ²	50 V	0.7–0.02 nA	0.217 ^{a)}	75	NA	NA	Mo-target, 50 kVp (peak at 17 keV)
PS-b-PPP: carbon SWNTs ^[97]	Drop casting	Photodiode Au/SWNT/LiF/Al	5 μm	3 × 3 mm ²	-150 V	NA	19.5 ^{b)}	3.89 × 10 ⁴	NA	NA	Cu-target (Kα 8.06 keV)
P3HT:PCBM + NP-GOS:TB ^[66]	Spray-coating	Hybrid-organic photodiode ITO/TFB/P3HT/ P3HT:PCBM:GOS:Tb/Al on a-Si:H TFT backplane	10 μm	1 cm ² (single device)	-10 V (-1 V μm ⁻¹)	4 × 10 ⁻⁴ mA cm ⁻²	7.34 ^{a)} (459 e ⁻ nGyair ⁻¹ mm ⁻²)	7.3 × 10 ^{3a)}	NA	400 ms	W-target, 70 kVp 2.5 mm Al filter
P3HT:PCBM:PBS QDs blend ^[26]	Spray-coating	Hybrid-organic photodiode ITO/P3HT:PCBM:PBS QDs/Al	2.6–30 μm	1 cm ²	1 V mm ⁻¹	10 ⁻⁵ –10 ⁻⁴ mA cm ⁻²	0.13 ^{b)} (8 e ⁻ nGyair ⁻¹ mm ⁻²)	NA	NA	>5 s	W-target 40 kVp
TIPS-pentacene ^[21]	Drop casting	Photoconductor Au/TIPS-pen/Au	100 nm	0.25 cm ²	0.2 V	NA	0.77 ^{a)}	7.7 × 10 ⁴	NA	>10 s	Mo-target 35 kVp (peak@17 keV) Synchrotron radiation (17 keV)
TIPS-pentacene ^[23]	Drop casting	Phototransistor	100 nm	0.25 cm ²	-3 V	NA	4.8	4.8 × 10 ^{3b)}	NA	>10 s	Mo-target 35 kVp (peak@17 keV)
PFO:Bi ₂ O ₃ NPs ^[25]	Spin coating	Photodiode Cr/Au/PFO:Bi ₂ O ₃ /MoO ₃ /Al	1 μm	0.16 mm ²	-80 V 80 V	200 nA cm ⁻² (3.6 × 10 ⁻³ A)	24 280 ^{a)}	2.4 × 10 ^{5a)} 2.8 × 10 ^{6a)}	NA	=5 ms NA	Mo-target, 35 kVp (Kα 17 keV)
P3HT:PCBM + Bi ₂ O ₃ NP ^[23]	Spin coating/ drop casting	Photodiode ITO/PEDOT:PSS/ P3HT:PCBM:Bi ₂ O ₃ /BCP/Al imager on a 256 × 256 a-Si:H TFTs backplane	10–30 μm 250 μm (imager)	0.68 cm ²	-10 V	10 ⁻⁴ –10 ⁻⁶ A cm ⁻²	3.9 × 10 ^{3a)}	1.7 × 10 ⁶ (3 × 10 ⁵ flex) 5.8 × 10 ⁴ (15 MV)	NA	NA	W-target 50 kVp LINAC (6 and 15 MV)
TIPGe-pentacene ^[28]	Drop casting	Phototransistor Au/TIPGe/Au	200 nm	0.25 cm ²	V _{DS} = -3, V _{GS} = -2 V	8 μA	17.8 ^{a)}	9.0 × 10 ⁵	1.66	NA	Mo-target, 35 kVp (Kα 17 keV)
P3HT:PCBM + Bi ₂ O ₃ NPs ^[20]	Power pellet pressing ^{b)}	Photoconductor: Au/ P3HT:PCBM:Bi ₂ O ₃ /Au imager in a 256 × 256 a-Si:H TFT backplane 98 μm pitch	0.1–1 mm 250 μm (imager)	1 cm ²	200 V	≈100 μA cm ⁻²	2.8 × 10 ^{3a)}	1.6 × 10 ⁵	NA	>10 s	W-target, 70 kVp 2.5 mm Al filter
TIPS-pentacene TIPGe-pentacene ^[30]	Drop casting	Photoconductor Au/TIPS(Ce)/Au	100–200 nm	4 × 4 mm ²	0.5 V	NA	3.2 ^{a)}	1.6 × 10 ⁵	12	<100 ms	W-target, 70 kVp Synchrotron radiation at 17 keV
PS:TIPS-pentacene ^[22]	BAMS	Phototransistor Au/Org/Au	40 nm	0.42 mm ²	V _{DS} = -20, V _{GS} = -15 V	NA	1.3 × 10 ⁴	3.2 × 10 ⁹	35	>10 s	Mo-target, 35 kVp (Kα 17 keV)

a) not reported by the authors, estimation based on published data; b) no solution grown method.

Table 4. Perovskite films.

Material	Growth method	Structure	Thickness	Active area	V _{bias}	I _{dark}	S _A [μC Gy _{air} ⁻¹ cm ⁻²]	S _V [μC Gy _{air} ⁻¹ cm ⁻³]	LoD [μC Gy _{air} ⁻¹ s ⁻¹]	Response time (cut-off)	X-ray Source
MAPbI ₃ [6]	Spin-coating	p-i-n photodiode	260–600 nm	NA	0V	NA	0.4–1.5 ^{a)}	14–25 × 10 ³	NA	20 ms	W-target, 75 kVp
	Spin-coating/ spray coating	Lateral photoconductor	60 μm	NA	80 V	NA	NA	NA	NA	(100 Hz)	Cu-target (Kα 8 keV)
CsFAMA[15]	Spin-coating	p-i-n photodiode	450 nm	6 mm ²	0 V 0.4 V	NA	3.7 98	8.2 × 10 ^{4b)} 2.2 × 10 ^{6a)}	NA	490 ms	Mo-target, 35 kVp (peak@17 keV)
	Spin-coating	Lateral photoconductor Au/Per/Au	NA	NA	10V	NA	3.2	NA	NA	NA	
MAPbI ₃ [6]	Sintering	Photodiode glass/ITO/ PEDOT:PSS/MAPbI ₃ /PCBM/ ZnO/Ag	700 μm to 1 mm	Ø 1/2 inch	0.2 V μm ⁻¹	6 μA cm ⁻²	2527	NA	48	NA	W-target, 70 kVp (peak@38 keV)
MAPbI ₃ [6]	Doctor blade	Photoconductor ITO/PI-MAPbI ₃ /MAPbI ₃ / PI-MAPbBr ₃ /a-Si TFT/ITO	830 μm	50 × 50 cm ²	10–200 V	≈10 ⁻² mA cm ⁻²	0.3–3.8 × 10 ³ (single pixel) 1.1 × 10 ⁴	1.3 × 10 ^{5a)}	NA	<50 ms	W-target, 100 kVp 3 mm Al filter
CsPbBr ₃ [67]	Hot-pressing ^{b)}	Schottky diode FTO/Per/Au	240 μm	9 mm ²	5 V mm ⁻¹	NA	5.57 × 10 ⁴	2.32 × 10 ^{6a)}	0.215	92 ms	W-target, 50 kVp (peak@30 keV)
CsPbBr ₃ QDs[64]	Inkjet printing	Photoconductor Au/Per/Au	20 nm	0.06 mm ²	0.1 V	0.01 nA	83 17.7 (flex) 1450 (low dose)	7.25 × 10 ^{8a)}	17.2	30 ms	Synchrotron radiation (100–2500 eV) Cu-target (Kα 8 keV)
CsPbBr ₃ [100]	Dissolution– recrystallization	Schottky structure Au/CsPbBr ₃ /ITO	18 μm	0.5 cm ²	0 V 0.11V	NA	470 1.7 × 10 ³	NA	0.053	NA	Cu-target, 35 kVp
CsPbBr ₃ [57]	Drop casting	Photoconductor Au/PERO/Au/PMMA capping	NA	Ø 5 mm	5 V	NA	NA	70	6 × 10 ³ μGy	NA	LINAC 6 MV and 25 MV
Cs ₂ TeI ₆ [59]	Electrostatic- assisted spray coating	Photodiode FTO/c-&m-TiO ₂ +Cs ₂ TeI ₆ / PTAA/Au	25 μm	NA	1 V (250 V·cm ⁻¹)	NA	19.2	7.68 × 10 ^{4a)}	NA	NA	40 kVp
CsPbBr ₃ [69]	Melt process ^{b)}	Photoconductor FTO/Per/Ga	250 μm	1 sq. in.	300 V	NA	1450	5.8 × 10 ^{5a)}	0.5		70 kVp 2mm Al filtered
CsFAMA[65]	Inkjet printing	p-i-n photodiode	3.7 μm	0.114 cm ²	0.1 V	0.3 μA cm ⁻²	59.9	1.62 × 10 ^{5a)}	12	248 ms	W-target 70 kVp 0.4 mm Al filter
MAPbI ₃ [102]	Pressing ^{b)}	Photoconductor Au/PCBM/perovskite wafer/Au	800 μm	0.09 cm ²	1 V 10 V	NA	2.20 × 10 ⁴ 1.22 × 10 ⁵	1.525 × 10 ^{6a)}	NA	NA	Ag-target, 40 kVp
(BA) ₂ (MA) ₂ Pb ₃ I ₁₀ (Pb ₃) ¹⁰¹	AVC	p-i-n photodiode ITO/PTAA/pero/C60/Au	470 nm	0.04 cm ²	0 V	1 nA cm ⁻²	13	2.76 × 10 ⁵	400	NA	Synchrotron radiation 8.05 and 10.9 keV

^{a)} not reported by the authors, estimation based on published data; ^{b)} no solution grown method.

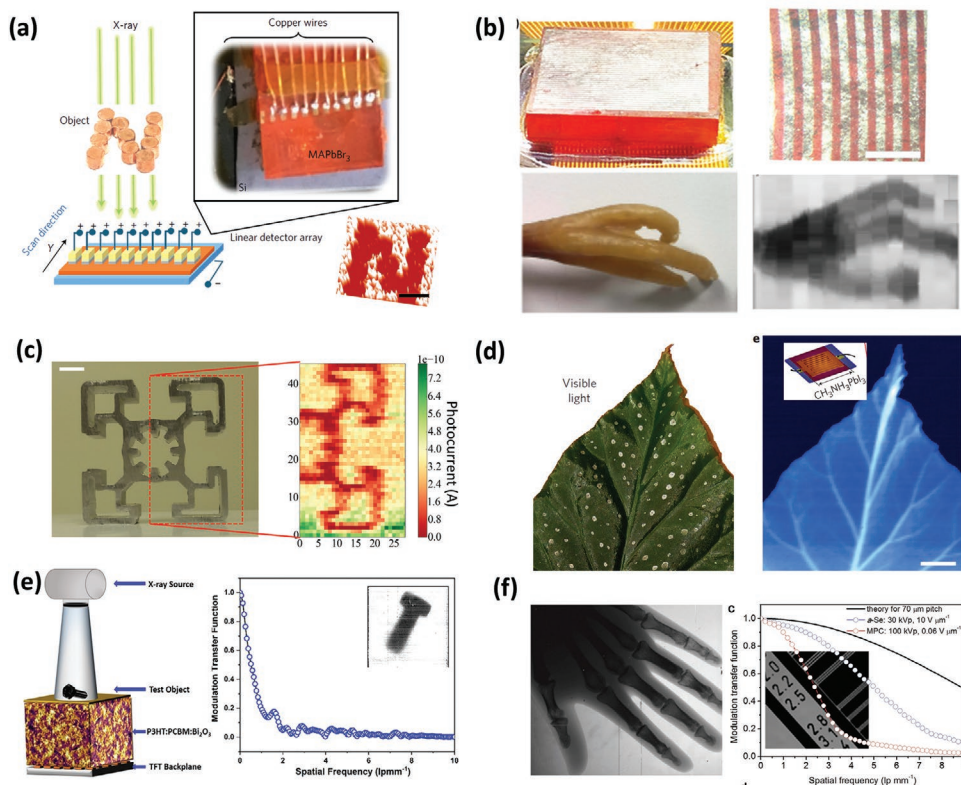


Figure 13. X-ray imaging performance: a) Schematics and picture of X-ray imaging with Si-integrated MAPbBr₃ single crystal detectors. The X-ray image of a “N-shaped logo” is also shown. Reproduced with permission.^[47] Copyright 2017, Springer Nature. b) Pictures of the PIN photodiodes array made of MAPbBr₃ single crystal. Scale bar is 1.5 mm. Bottom: optical and X-ray image of a chicken claw. Adapted with permission.^[87] Copyright 2018, Wiley-VCH. c) optical and X-ray image of a structured aluminum profile obtained with a full-organic TIPS-pentacene thin film flexible detector. Scale bar is 1 cm. Reproduced with permission.^[30] Copyright 2020, Frontiers Research Foundation. d) Optical and X-ray image of a leaf obtained with a 60 μm thick MAPbI₃ film photoconductor detector (the sketch of the device structure is in the inset). The scale bar is 1 cm. Reproduced with permission.^[16] Copyright 2015, Springer Nature. e) Left: schematic of the imager architecture where the BHJ:NPs 250 μm thick active layer is interfaced with an active matrix Si TFTs backplane. Right: Plot of MTF versus spatial resolution. The inset reports the X-ray image of a screw. Adapted with permission.^[70] Copyright 2019, American Chemical Society. f) Right: X-ray image of a hand phantom obtained with a 830 μm thick polycrystalline MAPbI₃ photoconductor blade coated onto a -Si:H TFT backplane. Right: MTF of the perovskite detector (red) compared to the theoretical values (black) and that of a conventional a-Se direct detector with the same pitch (blue). In the inset the X-ray image of a resolution phantom is shown. Reproduced with permission.^[6] Copyright 2017, Springer Nature.

cost-effective fabrication, scalability to large area systems, and the use of limited amounts of earth-abundant precursors. In particular, the human-tissue equivalence of organic material is a peculiar feature extremely relevant for their application in medical dosimetry.

This review portrays the most recent results on X-ray direct detectors fabricated from solution-grown organic semiconductors and perovskites, critically discussed by dividing them on the basis of the material form (single crystal or film). The fundamental principles underlying the X-ray detection processes are discussed together with the models presented in the literature to account for the observed behaviors. The overall presented results are impressive, showing how in few years, these two classes of materials have been able to achieve performance comparable (and in some cases surpassing) state-of-the-art traditional radiation detectors.

More research and more efforts are still needed to fully expand their potential and, as a future outlook, attention should be devoted to reducing the dark current (for both types of materials in their film form), so to improve the lowest detectable

dose (i.e., the LoD of the detectors). The radiation hardness of both types of detectors is still poorly addressed, even if it can be a very relevant parameter to consider when evaluating reliability, long-term use, and disposability issues.

Organic-based detectors would greatly benefit from further investigations targeting improvements of their efficiency, while the major bottleneck for perovskite-based devices is still represented by the limited stability of the material. In fact, in contrast to solar cells, an external bias is typically applied in X-ray detectors to optimize the charge generation and collection, and this can severely affect the long-term stability of perovskites. Developing new structure-function relationships specific to X-ray radiation detection and new models that analytically describe the physical processes underlying the radiation–perovskite interaction is a critical next step in advancing this field of research.

In summary, there is still a wealth of fundamental research and fabrication engineering that must be developed to reveal the full potential of organic/hybrid semiconductors and perovskites as a new paradigm in the emerging field of radiation detection. We hope that this review on the impressive and

exciting results achieved so far will stimulate and magnify such a research.

Acknowledgements

The authors acknowledge funding from INFN through the CSN5 FIRE project. This article is part of the *Advanced Materials Technologies* Hall of Fame article series, which recognizes the excellent contributions of leading researchers to the field of technology-related materials science.

Conflict of Interest

The authors declare no conflict of interest.

Keywords

organic semiconductors, perovskites, solution growth, X-ray detectors

Received: May 15, 2020

Revised: June 26, 2020

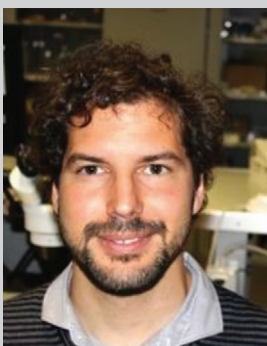
Published online: August 25, 2020

- [1] M. Spahn, *Nucl. Instrum. Methods Phys. Res., Sect. A* **2013**, 731, 57.
- [2] G. Zentai, *2008 IEEE International Workshop on Imaging Systems and Techniques*, IEEE, Crete **2008**, pp. 1–6.
- [3] R. P. Haff, N. Toyofuku, *Sens. Instrum. Food Qual.* **2008**, 2, 262.
- [4] M. Z. Kabir, M. Yunus, S. O. Kasap, O. Tournant, H. Mani, P. Gauthier, *Curr. Appl. Phys.* **2006**, 6, 393.
- [5] A. Owens, A. Peacock, *Nucl. Instrum. Methods Phys. Res., Sect. A* **2004**, 531, 18.
- [6] G. F. Knoll, *Radiation Detection and Measurements*, John Wiley and Sons, Inc., New York **2011**.
- [7] Z. Xiao, R. A. Kerner, L. Zhao, N. L. Tran, K. M. Lee, T.-W. Koh, G. D. Scholes, B. P. Rand, *Nat. Photon* **2017**, 11, 108.
- [8] C. Bao, Z. Chen, Y. Fang, H. Wei, Y. Deng, X. Xiao, L. Li, J. Huang, *Adv. Mater.* **2017**, 29, 1703209.
- [9] M. Kaltenbrunner, G. Adam, E. D. Głowacki, M. Drack, R. Schwödiauer, L. Leonat, D. H. Apaydin, H. Groiss, M. C. Scharber, M. S. White, N. S. Sariciftci, S. Bauer, *Nat. Mater.* **2015**, 14, 1032.
- [10] F. P. G. de Arquer, A. Armin, P. Meredith, E. H. Sargent, *Nat. Rev. Mater.* **2017**, 2, 16100.
- [11] H. Wei, J. Huang, *Nat. Commun.* **2019**, 10, 1066.
- [12] M. Ahmadi, T. Wu, B. Hu, *Adv. Mater.* **2017**, 29, 1605242.
- [13] S. De Wolf, J. Holovsky, S.-J. Moon, P. Löper, B. Niesen, M. Ledinsky, F.-J. Haug, J.-H. Yum, C. Ballif, *J. Phys. Chem. Lett.* **2014**, 5, 1035.
- [14] L. Dou, Y. (Micheal) Yang, J. You, Z. Hong, W.-H. Chang, G. Li, Y. Yang, *Nat. Commun.* **2014**, 5, 5404.
- [15] L. Basiricò, S. P. Senanayak, A. Ciavatti, M. Abdi-Jalebi, B. Fraboni, H. Siringhaus, *Adv. Funct. Mater.* **2019**, 29, 1902346.
- [16] S. Yakunin, M. Sytnyk, D. Krieger, S. Shrestha, M. Richter, G. J. Matt, H. Azimi, C. J. Brabec, J. Stangl, M. V. Kovalenko, W. Heiss, *Nat. Photon* **2015**, 9, 444.
- [17] M. Irimia-Vladu, E. D. Głowacki, G. Voss, S. Bauer, N. S. Sariciftci, *Mater. Today* **2012**, 15, 340.
- [18] D. Zhao, M. Xu, B. Xiao, B. Zhang, L. Yan, G. Zeng, A. Dubois, P. Sellin, W. Jie, Y. Xu, *J. Mater. Chem. A* **2020**, 8, 5217.
- [19] B. Fraboni, A. Ciavatti, F. Merlo, L. Pasquini, A. Cavallini, A. Quaranta, A. Bonfiglio, A. Fraleoni-Morgera, *Adv. Mater.* **2012**, 24, 2289.
- [20] L. Basirico, A. Ciavatti, M. Sibilìa, A. Fraleoni-Morgera, S. Trabatttoni, A. Sassella, B. Fraboni, *IEEE Trans. Nucl. Sci.* **2015**, 62, 1791.
- [21] L. Basiricò, A. Ciavatti, T. Cramer, P. Cosseddu, A. Bonfiglio, B. Fraboni, *Nat. Commun.* **2016**, 7, 13063.
- [22] I. Temiño, L. Basiricò, I. Fratelli, A. Tamayo, A. Ciavatti, M. Mas-Torrent, B. Fraboni, *Nat. Commun.* **2020**, 11, 2136.
- [23] H. M. Thirimanne, K. D. G. I. Jayawardena, A. J. Parnell, R. M. I. Bandara, A. Karalasingam, S. Pani, J. E. Huerdler, D. G. Lidzey, S. F. Tedde, A. Nisbet, C. A. Mills, S. R. P. Silva, *Nat. Commun.* **2018**, 9, 2926.
- [24] C. A. Mills, H. Al-Otaibi, A. Intaniwet, M. Shkunov, S. Pani, J. L. Keddie, P. J. Sellin, *J. Phys. D: Appl. Phys.* **2013**, 46, 275102.
- [25] A. Ciavatti, T. Cramer, M. Carroli, L. Basiricò, R. Fuhrer, D. M. De Leeuw, B. Fraboni, *Appl. Phys. Lett.* **2017**, 111, 183301.
- [26] G. N. Ankah, P. Büchele, K. Poulsen, T. Rauch, S. F. Tedde, C. Gimmler, O. Schmidt, T. Kraus, *Org. Electron.* **2016**, 33, 201.
- [27] J. E. Anthony, *Nat. Mater.* **2014**, 13, 773.
- [28] A. Ciavatti, L. Basiricò, I. Fratelli, S. Lai, P. Cosseddu, A. Bonfiglio, J. E. Anthony, B. Fraboni, *Adv. Funct. Mater.* **2019**, 29, 1806119.
- [29] M. J. Griffith, S. Cottam, J. Stamenkovic, J. A. Posar, M. Petasecca, *Front. Phys.* **2020**, 8, 22.
- [30] L. Basiricò, A. Ciavatti, I. Fratelli, D. Dreossi, G. Tromba, S. Lai, P. Cosseddu, A. Bonfiglio, F. Mariotti, C. Dalla Val, V. Bellucci, J. E. Anthony, B. Fraboni, *Front. Phys.* **2020**, 8, 13.
- [31] B. Fraboni, A. Fraleoni-Morgera, N. Zaitseva, *Adv. Funct. Mater.* **2016**, 26, 2276.
- [32] B. Fraboni, C. Femoni, I. Mencarelli, L. Setti, R. Di Pietro, A. Cavallini, A. Fraleoni-Morgera, *Adv. Mater.* **2009**, 21, 1835.
- [33] C. C. Stoumpos, C. D. Malliakas, J. A. Peters, Z. Liu, M. Sebastian, J. Im, T. C. Chasapis, A. C. Wibowo, D. Y. Chung, A. J. Freeman, B. W. Wessels, M. G. Kanatzidis, *Cryst. Growth Des.* **2013**, 13, 2722.
- [34] M. Brissaud, C. Dolin, J. Le Duigou, B. S. McArdle, J. N. Sherwood, *J. Cryst. Growth* **1977**, 38, 134.
- [35] H. Jiang, C. Kloc, *MRS Bull.* **2013**, 38, 28.
- [36] A. Fraleoni-Morgera, L. Benevoli, B. Fraboni, *J. Cryst. Growth* **2010**, 312, 3466.
- [37] B. Fraboni, A. Ciavatti, L. Basiricò, A. Fraleoni-Morgera, *Faraday Discuss.* **2014**, 174, 219.
- [38] A. Ciavatti, E. Capria, A. Fraleoni-Morgera, G. Tromba, D. Dreossi, P. J. Sellin, P. Cosseddu, A. Bonfiglio, B. Fraboni, *Adv. Mater.* **2015**, 27, 7213.
- [39] A. Ciavatti, P. J. Sellin, L. Basiricò, A. Fraleoni-Morgera, B. Fraboni, *Appl. Phys. Lett.* **2016**, 108, 153301.
- [40] G. Pipan, M. Bogar, A. Ciavatti, L. Basiricò, T. Cramer, B. Fraboni, A. Fraleoni-Morgera, *Adv. Mater. Interfaces* **2017**, 5, 1700925.
- [41] L. Carman, H. P. Martinez, L. Voss, S. Hunter, P. Beck, N. Zaitseva, S. A. Payne, P. Irkhin, H. H. Choi, V. Podzorov, *IEEE Trans. Nucl. Sci.* **2017**, 64, 781.
- [42] R. A. Laudise, C. Kloc, P. G. Simpkins, T. Siegrist, *J. Cryst. Growth* **1998**, 187, 449.
- [43] H. Wang, Z. Q. Xie, B. Yang, F. Z. Shen, Y. P. Li, Y. G. Ma, *CrystEngComm* **2008**, 10, 1252.
- [44] R. Zhuang, X. Wang, W. Ma, Y. Wu, X. Chen, L. Tang, H. Zhu, J. Liu, L. Wu, W. Zhou, X. Liu, Y. (Michael) Yang, *Nat. Photonics* **2019**, 13, 602.
- [45] C. Kloc, K. J. Tan, M. L. Toh, K. K. Zhang, Y. P. Xu, *Appl. Phys. A* **2009**, 95, 219.
- [46] M. I. Saidaminov, A. L. Abdelhady, B. Murali, E. Alarousu, V. M. Burlakov, W. Peng, I. Dursun, L. Wang, Y. He, G. Maculan, A. Goriely, T. Wu, O. F. Mohammed, O. M. Bakr, *Nat. Commun.* **2015**, 6, 7586.
- [47] W. Wei, Y. Zhang, Q. Xu, H. Wei, Y. Fang, Q. Wang, Y. Deng, T. Li, A. Gruverman, L. Cao, J. Huang, *Nat. Photon* **2017**, 11, 315.

- [48] D. Shi, V. Adinolfi, R. Comin, M. Yuan, E. Alarousu, A. Buin, Y. Chen, S. Hoogland, A. Rothenberger, K. Katsiev, Y. Losovyj, X. Zhang, P. A. Dowben, O. F. Mohammed, E. H. Sargent, O. M. Bakr, *Science* **2015**, *347*, 519.
- [49] H. Wei, Y. Fang, P. Mulligan, W. Chuirazzi, H.-H. Fang, C. Wang, B. R. Ecker, Y. Gao, M. A. Loi, L. Cao, J. Huang, *Nat. Photon* **2016**, *10*, 333.
- [50] S. Yakunin, D. N. Dirin, Y. Shynkarenko, V. Morad, I. Cherniukh, O. Nazarenko, D. Kreil, T. Nauser, M. V. Kovalenko, *Nat. Photon* **2016**, *10*, 585.
- [51] H. Wei, D. DeSantis, W. Wei, Y. Deng, D. Guo, T. J. Savenije, L. Cao, J. Huang, *Nat. Mater.* **2017**, *16*, 826.
- [52] H. Zhang, F. Wang, Y. Lu, Q. Sun, Y. Xu, B.-B. Zhang, W. Jie, M. G. Kanatzidis, *J. Mater. Chem. C* **2020**, *8*, 1248.
- [53] W. Pan, H. Wu, J. Luo, Z. Deng, C. Ge, C. Chen, X. Jiang, W.-J. Yin, G. Niu, L. Zhu, L. Yin, Y. Zhou, Q. Xie, X. Ke, M. Sui, J. Tang, *Nat. Photonics* **2017**, *11*, 726.
- [54] A. Intaniwet, C. A. Mills, M. Shkunov, H. Thiem, J. L. Keddie, P. J. Sellin, *J. Appl. Phys.* **2009**, *106*, 064513.
- [55] A. Intaniwet, J. L. Keddie, M. Shkunov, P. J. Sellin, *Org. Electron.* **2011**, *12*, 1903.
- [56] F. A. Boroumand, M. Zhu, A. B. Dalton, J. L. Keddie, P. J. Sellin, J. J. Gutierrez, *Appl. Phys. Lett.* **2007**, *91*, 033509.
- [57] M. Bruzzi, C. Talamonti, N. Calisi, S. Caporali, A. Vinattieri, *APL Mater.* **2019**, *7*, 051101.
- [58] Y. Diao, L. Shaw, Z. Bao, S. C. B. Mannsfeld, *Energy Environ. Sci.* **2014**, *7*, 2145.
- [59] Y. Xu, B. Jiao, T.-B. Song, C. C. Stoumpos, Y. He, I. Hadar, W. Lin, W. Jie, M. G. Kanatzidis, *ACS Photonics* **2019**, *6*, 196.
- [60] P. Büchele, M. Richter, S. F. Tedde, G. J. Matt, G. N. Anka, R. Fischer, M. Biele, W. Metzger, S. Lilliu, O. Bikondoa, J. E. Macdonald, C. J. Brabec, T. Kraus, U. Lemmer, O. Schmidt, *Nat. Photonics* **2015**, *9*, 843.
- [61] Y. C. Kim, K. H. Kim, D.-Y. Son, D.-N. Jeong, J.-Y. Seo, Y. S. Choi, I. T. Han, S. Y. Lee, N.-G. Park, *Nature* **2017**, *550*, 87.
- [62] A. Pérez-Rodríguez, I. Temiño, C. Ocal, M. Mas-Torrent, E. Barrena, *ACS Appl. Mater. Interfaces* **2018**, *10*, 7296.
- [63] I. Temiño, F. G. Del Pozo, M. R. Ajayakumar, S. Galindo, J. Puigdollers, M. Mas-Torrent, *Adv. Mater. Technol.* **2016**, *1*, 1600090.
- [64] J. Liu, B. Shabbir, C. Wang, T. Wan, Q. Ou, P. Yu, A. Tadich, X. Jiao, D. Chu, D. Qi, D. Li, R. Kan, Y. Huang, Y. Dong, J. Jasieniak, Y. Zhang, Q. Bao, *Adv. Mater.* **2019**, *31*, 1901644.
- [65] H. Mescher, F. Schackmar, H. Eggers, T. Abzieher, M. Zuber, E. Hamann, T. Baumbach, B. S. Richards, G. Hernandez-Sosa, U. W. Paetzold, U. Lemmer, *ACS Appl. Mater. Interfaces* **2020**, *12*, 15774.
- [66] S. Shrestha, R. Fischer, G. J. Matt, P. Feldner, T. Michel, A. Osvet, I. Levchuk, B. Merle, S. Golkar, H. Chen, S. F. Tedde, O. Schmidt, R. Hock, M. Rührig, M. Göken, W. Heiss, G. Anton, C. J. Brabec, *Nat. Photonics* **2017**, *11*, 436.
- [67] W. Pan, B. Yang, G. Niu, K.-H. Xue, X. Du, L. Yin, M. Zhang, H. Wu, X.-S. Miao, J. Tang, *Adv. Mater.* **2019**, *31*, 1904405.
- [68] M. Hu, S. Jia, Y. Liu, J. Cui, Y. Zhang, H. Su, S. Cao, L. Mo, D. Chu, G. Zhao, K. Zhao, Z. Yang, S. F. Liu, *ACS Appl. Mater. Interfaces* **2020**, *12*, 16592.
- [69] G. J. Matt, I. Levchuk, J. Knüttel, J. Dallmann, A. Osvet, M. Sytnyk, X. Tang, J. Elia, R. Hock, W. Heiss, C. J. Brabec, *Adv. Mater. Interfaces* **2020**, *7*, 1901575.
- [70] K. D. G. I. Jayawardena, H. M. Thirimanne, S. F. Tedde, J. E. Huedler, A. J. Parnell, R. M. I. Bandara, C. A. Mills, S. R. P. Silva, *ACS Nano* **2019**, *13*, 6973.
- [71] K.-J. Baeg, M. Binda, D. Natali, M. Caironi, Y.-Y. Noh, *Adv. Mater.* **2013**, *25*, 4267.
- [72] F. Chen, K. Wang, Y. Fang, N. Allec, G. Belev, S. O. Kasap, K. S. Karim, *IEEE Sens. J.* **2011**, *11*, 505.
- [73] S. Lai, P. Cosseddu, L. Basiricò, A. Ciavatti, B. Fraboni, A. Bonfiglio, *Adv. Electron. Mater.* **2017**, *3*, 1600409.
- [74] K. Wang, F. Chen, N. Allec, F. Yuan, G. Belev, S. Kasap, K. S. Karim, *IEEE Electron. Device Lett.* **2011**, *32*, 782.
- [75] W. Shockley, *J. Appl. Phys.* **1938**, *9*, 635.
- [76] S. Ramo, *Proceed. IRE* **1939**, *27*, 584.
- [77] M. Z. Kabir, S. Kasap, in *Springer Handbook of Electronic and Photonic Materials*, (Eds.: S. Kasap, P. Capper), Springer International Publishing, Cham **2017**, p. 1.
- [78] S. O. Kasap, *J. Phys. D: Appl. Phys.* **2000**, *33*, 2853.
- [79] H. Tsai, F. Liu, S. Shrestha, K. Fernando, S. Tretiak, B. Scott, D. T. Vo, J. Strzalka, W. Nie, *Sci. Adv.* **2020**, *6*, eaay0815.
- [80] S. Kasap, J. B. Frey, G. Belev, O. Tournant, H. Mani, J. Greenspan, L. Laperrriere, O. Bubon, A. Reznik, G. DeCrescenzo, K. S. Karim, J. A. Rowlands, *Sensors* **2011**, *11*, 5112.
- [81] D. R. Shearer, M. Bopaiah, *Health Phys.* **2000**, *79*, S20.
- [82] I. Clairand, J.-M. Bordy, E. Carinou, J. Daures, J. Debros, M. Denozière, L. Donadille, M. Ginjaume, C. Itié, C. Koukorava, S. Krim, A.-L. Lebacqz, P. Martin, L. Struelens, M. Sans-Merce, F. Vanhavere, *Radiat. Meas.* **2011**, *46*, 1252.
- [83] M. Thompson, S. L. R. Ellison, R. Wood, *Pure Appl. Chem.* **2002**, *74*, 835.
- [84] L. A. Currie, *Anal. Chem.* **1968**, *40*, 586.
- [85] V. Podzorov, E. Menard, A. Borissov, V. Kiryukhin, J. A. Rogers, M. E. Gershenson, *Phys. Rev. Lett.* **2004**, *93*, 086602.
- [86] H. Najafav, B. Lee, Q. Zhou, L. C. Feldman, V. Podzorov, *Nat. Mater.* **2010**, *9*, 938.
- [87] X. Wang, D. Zhao, Y. Qiu, Y. Huang, Y. Wu, G. Li, Q. Huang, Q. Khan, A. Nathan, W. Lei, J. Chen, *Phys. Status Solidi RRL* **2018**, *12*, 1800380.
- [88] X. Geng, Q. Feng, R. Zhao, T. Hirtz, G. Dun, Z. Yan, J. Ren, H. Zhang, R. Liang, H. Tian, D. Xie, Y. Yang, T.-L. Ren, *IEEE Electron. Device Lett.* **2020**, *41*, 256.
- [89] L. Li, X. Liu, H. Zhang, B. Zhang, W. Jie, P. J. Sellin, C. Hu, G. Zeng, Y. Xu, *ACS Appl. Mater. Interfaces* **2019**, *11*, 7522.
- [90] X. Zheng, W. Zhao, P. Wang, H. Tan, M. I. Saidaminov, S. Tie, L. Chen, Y. Peng, J. Long, W. Zhang, *J. Energy Chem.* **2020**, *249*, 299.
- [91] J. A. Steele, W. Pan, C. Martin, M. Keshavarz, E. Debroye, H. Yuan, S. Banerjee, E. Fron, D. Jonckheere, C. W. Kim, W. Baekelant, G. Niu, J. Tang, J. Vanacken, M. V. der Auweraer, J. Hofkens, M. B. J. Roeffaers, *Adv. Mater.* **2018**, *30*, 1804450.
- [92] Y. Zhang, Y. Liu, Z. Xu, H. Ye, Z. Yang, J. You, M. Liu, Y. He, M. G. Kanatzidis, S. (Frank) Liu, *Nat. Commun.* **2020**, *11*, 2304.
- [93] Z. Xu, X. Liu, Y. Li, X. Liu, T. Yang, C. Ji, S. Han, Y. Xu, J. Luo, Z. Sun, *Angew. Chem.* **2019**, *131*, 15904.
- [94] A. Intaniwet, C. A. Mills, P. J. Sellin, M. Shkunov, J. L. Keddie, *ACS Appl. Mater. Interfaces* **2010**, *2*, 1692.
- [95] S. Lai, G. Casula, P. Cosseddu, L. Basiricò, A. Ciavatti, F. D'Annunzio, C. Loussert, V. Fischer, B. Fraboni, M. Barbaro, A. Bonfiglio, *Org. Electron.* **2018**, *58*, 263.
- [96] A. Intaniwet, C. A. Mills, M. Shkunov, P. J. Sellin, J. L. Keddie, *Nanotechnology* **2012**, *23*, 235502.
- [97] H. Han, S. Lee, J. Seo, C. Mahata, S. H. Cho, A.-R. Han, K.-S. Hong, J.-H. Park, M.-J. Soh, C. Park, T. Lee, *Nanoscale Res. Lett.* **2014**, *9*, 610.
- [98] J. Guo, Y. Xu, W. Yang, B. Zhang, J. Dong, W. Jie, M. G. Kanatzidis, *J. Mater. Chem. C* **2019**, *7*, 8712.
- [99] Y. He, L. Matei, H. J. Jung, K. M. McCall, M. Chen, C. C. Stoumpos, Z. Liu, J. A. Peters, D. Y. Chung, B. W. Wessels, M. R. Wasielewski, V. P. Dravid, A. Burger, M. G. Kanatzidis, *Nat. Commun.* **2018**, *9*, 1609.
- [100] C. Ji, S. Wang, Y. Wang, H. Chen, L. Li, Z. Sun, Y. Sui, S. Wang, J. Luo, *Adv. Funct. Mater.* **2020**, *30*, 1905529.
- [101] Z. Gou, S. Huanglong, W. Ke, H. Sun, H. Tian, X. Gao, X. Zhu, D. Yang, P. Wangyang, *Phys. Status Solidi RRL* **2019**, *13*, 1900094.
- [102] M. Hu, S. Jia, Y. Liu, J. Cui, Y. Zhang, H. Su, S. Cao, L. Mo, D. Chu, G. Zhao, K. Zhao, Z. Yang, S. F. Liu, *ACS Appl. Mater. Interfaces* **2020**, *12*, 16592.



Laura Basiricò received the M.S. degree in Physics from the University of Bologna, Bologna, Italy, in 2008. In 2009, she joined the University of Cagliari with the Department of Electrical and Electronic Engineering as Ph.D student. She received the Ph.D. degree in 2012. Currently and since 2013 she is a Researcher and Adjunct Professor at the Department of Physics and Astronomy, University of Bologna, Italy. Her research interests concern flexible and organic electronics, electronic devices for sensing applications and in particular for ionizing radiation detection, smart devices based on advanced materials and technologies.



Andrea Ciavatti received the M.Sc. Degree in Physics (2010) and the Ph.D in Physics (2015) at the University of Bologna, working on organic crystals for sensing applications. Among 2017 and 2018 he worked at “Istituto di Nanoscienze–CNR” and “National Enterprise for nanoScience and nano-Technology” in Pisa on the design and fabrication of THz lasers. Since 2015, he is a Researcher at the Department of Physics and Astronomy of University of Bologna. His research interests concern the electrical and photonic characterization of advanced materials and devices: flexible and large-area sensors for ionizing radiations based on organic and hybrid materials.



Beatrice Fraboni, Full Professor of Physics at the Department of Physics and Astronomy of the University of Bologna, holds a Master in Microelectronics (University of Cambridge, UK) and a PhD in Physics (University of Bologna, IT). She served as Rector's Delegate for International Relations of the University of Bologna (2015–2019) and presently is the Director of the “Collegio Superiore”; She coordinated several international and national research projects, published over 170 papers and holds 13 patents. Her research is focused on the opto-electronic transport properties of advanced organic and inorganic semiconducting materials and nano-devices for sensing applications.